

# DYNAMIC SILICON NANOPHOTONIC DEVICES

A Dissertation

Presented to the Faculty of the Graduate School

of Cornell University

In Partial Fulfillment of the Requirements for the Degree of

Doctor of Philosophy

by

Stefan Francis Preble

August 2007

© 2007 Stefan Francis Preble

# DYNAMIC SILICON NANOPHOTONIC DEVICES

Stefan Francis Preble, Ph. D.

Cornell University 2007

This dissertation is driven by a vision to continue improvements in system functionality by alleviating bottlenecks in interconnects and enabling the processing of large amounts of information on a chip. Light was the key for achieving long-haul interconnects 35 years ago and is now becoming the key for achieving high speed data communications on smaller scales [1-3]. The ultimate goal of this research is continue this trend to the smallest possible scale by developing a complex integrated Silicon Nanophotonic chip. Here I will present some of the building blocks for such a chip.

This dissertation is divided in five chapters, organized as follows. Chapter 1 gives an overview of why optical interconnects are needed on the chip scale. Then it discusses the challenges and the advantages of using a Silicon platform for such a photonic chip. We then provide a solution to the challenges by using compact resonators to dramatically increase light-matter interaction.

In Chapter 2 we demonstrate one of the most basic building blocks of a silicon nanophotonic chip – an all-optical modulator, where one beam of light controls the propagation of another. First we present low-powered all-optical modulation using a one-dimensional photonic crystal nanocavity. Then we demonstrate ultra-fast modulation using a ring resonator device with an integrated PIN diode. The diode is used to dramatically increase the speed of typical silicon modulators to at least 20 Gbit/s.

In Chapter 3 we discuss using evolutionary algorithms to design silicon nanophotonic devices that outperform human designs. In order to demonstrate the promise of evolutionary algorithms we present an example that designs a photonic crystal with a bandgap that is larger than previous human designs.

In Chapter 4 we present a new technique for achieving wavelength conversion where the wavelength of light confined in a resonator is changed by dynamically tuning the resonator. We discuss theoretically how this occurs and then demonstrate it experimentally using a ring resonator device.

Finally in Chapter 5, we demonstrate photonic transitions where light is transitioned between the discrete states of a resonator, in analogy to electronic transitions in an atom.

## **BIOGRAPHICAL SKETCH**

Stefan Francis Preble grew up in and near Hartford, CT. He graduated from the Rochester Institute of Technology with a Bachelors Degree in Electrical Engineering in 2002. He was a teaching assistant during his senior year and also conducted research in optical MEMS under the direction of Professor David Sumberg. Before that he was an intern at Sonalysts, Inc. and Texas Instruments, Inc. He joined Professor Michal Lipson's nanophotonics group at Cornell University in July 2002. Stefan focused on several research areas as a Ph.D. student including evolutionary algorithms, photonic crystals, and active silicon nanophotonic devices.

*I dedicate this Dissertation*

*To my wife, Kristin, for all of her loving support.*

*To my son, Ray, for bringing more joy into my life than I could have ever imagined.*

## ACKNOWLEDGMENTS

My five years as a Ph.D. student at Cornell University in the nanophotonics group have had a wonderful and profound impact on my life. The experience has given me an excellent foundation for my future life and career. There are so many great opportunities at this institution and I feel lucky to have had the privilege to access them. And a great institution is nothing without its people, who I would like to acknowledge here. I am making a strong effort to acknowledge all of them and I apologize in advance if I may have forgotten someone.

First I would like to thank my advisor, Professor Michal Lipson. It was a rare opportunity to have started in her group at the beginning of her career. It gave me wonderful insight into what it takes to make from scratch a very successful research team. I am grateful to her for giving me that opportunity and for her guidance.

I would also like to thank Professor Hod Lipson for his guidance on evolutionary algorithms. Without his help I would not have explored and had been successful in such an interesting research area.

I would like to thank Professors Alexander Gaeta and Clifford Pollock for being part of my special committee. Their fruitful comments were of great value.

I sincerely thank the other “founders” of the nanophotonics group, Vilson Almeida, Roberto Panepucci, and Carlos Barrios. I really appreciate their wise and very generous assistance at the initial onset of my degree. I especially thank Vilson for all of the training he gave me on experimental measurement techniques and for the help with my initial results.

I would like to thank my friend Brad Schmidt. I really value our initial collaborations in the first year of our degrees and for all of your support.

I would also like to thank Professor David Sumberg at the Rochester Institute of Technology for introducing me to the field and giving me my first research experiences.

Lastly, I would like to thank all of the other past and present members of the nanophotonics group for their friendship and support: Sameer Pradhan, Jagat Shakya, Christina Manolatu, Po Dong, Qianfan Xu, Jacob Robinson, Sasha Gondarenko, Long Chen, Sasikanth Manipatruni, Kyle Preson, Arthur Nitkowski, Nick Sherwood Droz and Linnell Martinez.



## TABLE OF CONTENTS

CHAPTER 1 - SILICON NANOPHOTONICS INTRODUCTION.....	1
1.1    SILICON OPTICAL INTERCONNECTS .....	1
1.2    PASSIVE SILICON NANOPHOTONIC DEVICES.....	3
1.3    SILICONS OPTICAL PROPERTIES .....	3
1.4    RESONATOR: KEY TO ACTIVE DEVICES.....	5
1.5    SUMMARY .....	8
CHAPTER 2 - ALL-OPTICAL SWITCHING AND MODULATION .....	10
2.1    INTRODUCTION .....	10
2.2    PHOTONIC CRYSTAL DEVICE .....	12
2.2.1 <i>SLOW SWITCHING</i> .....	15
2.2.2 <i>FAST SWITCHING</i> .....	23
2.3    ULTRA-FAST SWITCHING USING A DIODE.....	24
2.4    SUMMARY .....	32
CHAPTER 3 - EVOLUTIONARY ALGORITHMS FOR NANOPHOTONICS .....	33
3.1    INTRODUCTION .....	33
3.2    MAXIMIZING PHOTONIC CRYSTAL BANDGAP.....	34
3.3    METHODOLOGY .....	36
3.4    RESULTS AND DISCUSSION.....	44
3.5    SUMMARY .....	53
CHAPTER 4 - ADIABATIC WAVELENGTH CONVERSION .....	54
4.1    INTRODUCTION .....	54
4.2    THEORY AND SIMULATIONS .....	55

4.3	EXPERIMENTAL METHODS .....	62
4.4	RESULTS/DISCUSSION.....	65
4.5	SUMMARY .....	72
CHAPTER 5 - NON-ADIABATIC WAVELENGTH CONVERSION .....		73
5.1	INTRODUCTION .....	73
5.2	DEVICE .....	75
5.3	RESULTS/DISCUSSION.....	77
5.4	SUMMARY .....	84
REFERENCES .....		86

## LIST OF FIGURES

Figure 1.1. Optical interconnect timeline for various length scales (from [3]).	2
Figure 1.2. Schematic of a resonator showing that light traverses back and forth.	5
Figure 1.3. Schematic of a ring resonator	6
Figure 2.1. Scanning electron micrograph of the top-view of an one-dimensional photonic crystal nanocavity embedded in a Silicon waveguide (from [38]).	13
Figure 2.2. Measured and fitted transmission of the one-dimensional photonic crystal nano-cavity device (from [38]).	14
Figure 2.3. Example probe transmission before and after an 8 nm blue-shift of the cavity spectrum, demonstrating that a probe signal with a fixed wavelength ( $\lambda_{\text{probe}}=1.532$ nm in this example) can be modulated from off to on (from [38]).	15
Figure 2.4. Schematic of the pump-and-probe setup. A nanosecond dye laser is used to pump the device. A tunable laser is used to probe the device. Probe light transmitted thru the device is collected at the output of the waveguide and fed into a high-speed photodetector (from [38]).	16
Figure 2.5. Temporal response of probe at $\lambda_{\text{probe}} = 1532$ nm (below resonance). The pump is not to scale and is only for reference (from [38]).	18
Figure 2.6. Temporal response of probe at $\lambda_{\text{probe}} = 1535.5$ nm (Half-width-at-half-maximum below resonance). The pump is not to scale and is only for reference (from [38]).	18
Figure 2.7. Temporal response of probe at $\lambda_{\text{probe}} = 1539.5$ nm (on resonance). The pump is not to scale and is only for reference (from [38]).	19
Figure 2.8. Temporal response of a probe signal for two different probe wavelengths (on resonance and below resonance) using a one-dimensional photonic crystal nanocavity (from [41]).	23

Figure 2.9. Schematic drawing of the PIN ring resonator device used for all-optical modulation. A reverse bias is applied across the ring in order to extract carriers quickly. ....	25
Figure 2.10. PIN diode ring resonator fabrication process. All of the masks are defined using electron-beam lithography.....	25
Figure 2.11. Passive measurement of the spectrum of the PIN ring resonator device. $\lambda_{\text{pump}}$ is wavelength at which the pump beam operates and is tuned to one of the rings resonances. The inset shows the probe resonance where several probe wavelengths are indicated and are referred to.....	26
Figure 2.12. Carrier extraction time as a function of reverse-bias voltage. The inset shows the temporal probe signal for reverse-bias $V = 4\text{V}$ and the exponential fit used to obtain the extraction time ( $1/e$ point) (from [26]).....	28
Figure 2.13. Experimental (solid) and theoretical (dashed) temporal response of the probe signal with reverse-bias $V = 10\text{ V}$ . The inset shows the required switching energy (Pump Energy Dissipated) needed to maintain the same modulation depth for different reverse biases (from [26]). ....	29
Figure 3.1. A unit cell discretized onto a $32 \times 32$ grid and its associated binary string. The binary string encodes the unit cell row –by- row. Each pixel in the unit cell is assigned to be high (1) or low (0) dielectric material (from [54]). ....	37
Figure 3.2. (a) Illustration of an example $10 \times 10$ unit cell ( $32 \times 32$ is used with the evolutionary algorithm) and a top-down tree that can be used to construct this unit cell. The black (white) pixels are high (low) index material. The numbers label the perimeter of the unit cell. Starting at the top of the tree and going down, each split, a dividing line uniquely defined by two perimeter pixels, sections the unit cell into ever-smaller areas. The terminal nodes assign dielectric material	

(i.e. high or low) to these areas. Next to each terminal node is an illustration of the result. Light-gray coloring designates the sub-area that has been defined by the splits (i.e. the terminal nodes sibling ‘acts’ on this light-gray area). The complete unit cell is obtained by combining all of the sub-areas into one. (b) Illustration of an example 10x10 unit cell (32x32 is used with the evolutionary algorithm) and a bottom-up tree that can be used to construct this unit cell. The numbers around the unit-cell label the x-y grid. Starting at the bottom of the tree and going up, rectangles defined by a width, height, center and index are combined using boolean AND and OR operator nodes. The illustrations next to the nodes show how the rectangles are defined and combined to obtain the unit cell. The light-gray coloring indicates that those pixels are undefined and the boolean operators subsequently have no effect on them (i.e. defaults to OR). If there are any undefined pixels in the resulting unit cell, they are automatically set to be low index material (from [54])......38

Figure 3.3. Band diagram of a randomly generated photonic crystal with no bandgap.

The vertical axis is the frequencies normalized to  $(c/a)$  where ‘c’ is the speed of light and ‘a’ is the lattice period. The horizontal axis are the brillouin zone points. The inset shows the reciprocal lattice and the corresponding Brillouin zone points. The shaded light-gray boxes indicate the areas where the two bands overlap each other. The bounds of the boxes are obtained from the points in the band diagram where the top band is below the top of band 1. The height of the boxes is always the same; it’s defined from the bottom of band 2 (here at the X1 point) to the top of band 1 (here at the M point). The width is from the left-most to the right-most points (including the interpolated ‘half-way’ points) that fall

below the top of band 1. The total overlap area (Eq. (3.2)) can be obtained from the sum of the areas of the individual shaded boxes (from [54]).	41
Figure 3.4. An example rectangle that spans from point 1 in the ‘main’ unit-cell to points in the neighboring unit-cells. This representation is equivalent to a rectangle that spans the corners of the ‘main’ unit-cell (from [54]).	44
Figure 3.5. Photonic crystals and unit-cells (insets) created by the SUS evolutionary algorithm. From left to right: Bitmap Representation (5.12% Bandgap), Bottom up tree (30.86% Bandgap), Top down tree (31.89% Bandgap) (from [54]).	45
Figure 3.6. Band diagram of the photonic crystal discovered by the SUS evolutionary algorithm using a top down tree representation. The vertical axis is the frequencies normalized to $(c/a)$ where ‘c’ is the speed of light and ‘a’ is the lattice period. The horizontal axis is the brillouin zone points. The inset shows the reciprocal lattice and the corresponding Brillouin zone points (from [54]).	46
Figure 3.7. Photonic crystal and the unit-cell (indent) obtained using the bitmap representation with a 16x16 grid. The bandgap of the photonic crystal is 21.92% (from [54]).	47
Figure 3.8. Search performance of the SUS evolutionary algorithm. (a) Best fitness as a function of generation for each of the chromosome representations, (b) Average hamming distance as a function of generation. The curves were smoothed for presentation purposes. Error bars are derived from three independent runs started from randomized initial populations.	48
Figure 3.9. Photonic crystals and unit-cells (insets) created by the deterministic crowding evolutionary algorithm. From left to right: Bitmap Representation (21.32% Bandgap), Bottom up tree (29.7% Bandgap), Top down tree (30.73% Bandgap) (from [54]).	49

Figure 3.10. Performance metrics for the deterministic crowding algorithm with the different chromosome representations. Comparisons to a random search algorithm and parallel hill climbing algorithm (only for the bitmap approach) are shown. a) Best fitness as a function of generation. The ordering in the legend corresponds with the ordering of the fitness's on the graph (from best to worst). b) Average hamming distance as a function of generation. The curves were smoothed for presentation purposes. The left graph includes deterministic crowding and parallel hill climber. The right includes only random searches. Error bars are derived from three independent runs started from randomized initial populations.....	50
Figure 3.11. Best human designed photonic crystal with a bandgap of 28.35%. The photonic crystal is a square lattice of square air (index -1) holes of width and height $0.8 \cdot a$ ( $a$ is the periodicity of the lattice) embedded in a background of high index material (index - 3.4).....	53
Figure 4.1. Photonic crystal resonator used for wavelength conversion (Black – $n=2.75$ , White – Air). Light is launched into the line-defect waveguide and monitored in the center of the resonator.....	55
Figure 4.2. Envelope of the y-component of the electric field in the center of the photonic crystal resonator. Solid red line: Time response of the unmodulated resonator. Blue dashed line: Time response of the modulated resonator. Top: The time dependence of the index of refraction of the background material.....	56
Figure 4.3. Spectra of the light in the resonator in the unmodulated (red solid line) and the modulated (blue dashed line) cases. A wavelength shift of $\Delta\lambda=-5.2$ nm is obtained when the index is reduced by $\Delta n=-0.01$ .....	57

Figure 4.4. Zoom in of field shown in Figure 4.2 during the refractive index change at $t=3\text{ps}$ . It is clear that the energy in the cavity increases during the wavelength conversion process when the refractive index reduces.....	60
Figure 4.5. Change in energy in the cavity, change in wavelength and change in $E/\omega$ for different refractive index reductions. This shows that $\Delta(E/\omega)$ is an adiabatic invariant. ....	60
Figure 4.6. Scanning electron micrograph of a silicon ring resonator side-coupled to a waveguide (adapted from [17])......	63
Figure 4.7. Experimental set-up used to measure the wavelength-conversion process. OSA, optical spectrum analyser; PC, polarization controller; OPO, optical parametric oscillator; BBO, beta-barium borate crystal. The pump (illuminating the top of the resonator) is used to induce a dynamic change in the cavity, while the probe light (supplied by the OPO) is confined in the ring resonator (from [78]). ....	63
Figure 4.8. Wavelength conversion dependence on cavity detuning. a–d, Transmission spectra for four different detunings of the incident probe light wavelength relative to the cavity mode. Maximum conversion occurs when the probe is tuned to be on resonance, the dashed line is when the probe input power is reduced by 4.6 dB (a). The final wavelength is determined only by the degree of dynamic cavity change. e, Illustration of the wavelength-conversion process. f, The peak transmission of the probe when the pump is off. The four initial probe wavelengths (a-d) are indicated. (from [78]). ....	65
Figure 4.9. Dependence of the measured wavelength change with the absorbed pump energy (square dots – measured, solid line – linear fit). a-b, The insets show the transmitted probe power vs. wavelength relative to the initial cavity resonance for	



absorbed pump energies of 0.419 pJ (upper-left inset,  $\lambda_{\text{initial}}-\lambda_{\text{final}}=0.339$  nm, Induced Carrier Concentration  $\Delta N=1.65 \times 10^{17}$  cm<sup>-3</sup>) and 1.38 pJ (lower-right inset,  $\lambda_{\text{initial}}-\lambda_{\text{final}}=2.08$  nm, Induced Carrier Concentration  $\Delta N=1.39 \times 10^{18}$  cm<sup>-3</sup>), respectively. (from [78]).....67

Figure 4.10. On/off conversion efficiency dependence on wavelength change. The solid line shows our theoretical calculations and the square dots show our experimental conversion efficiency results. The maximum conversion efficiency (34%) was extrapolated from a fit of the experimental data. Free-carrier absorption reduces the conversion efficiency for increasing wavelength changes. (from [78]) .....68

Figure 4.11. Relative conversion efficiency as a function of the cavities transition time from its initial to final state. The transition time is normalized to the photon lifetime of the cavity. The solid line is an exponential decay fit to data calculated using two-dimensional finite difference time domain simulations. a-b, The insets show the measured probe power with two different pump pulse durations (cavity transition times). (from [78]) .....70

Figure 5.1. Illustration of the adiabatic and non-adiabatic wavelength conversion process using an infinite potential well analogy. ....73

Figure 5.2. Illustration that the spectral response of the resonators change must overlap many of the cavities modes in order to induce photonic transitions. ....74

Figure 5.3. Microscope image of the large ring resonator with input, thru and drop ports (from [86]).....75

Figure 5.4. Quasi-TM transmission of the through and drop ports of the ring resonator. ....76

Figure 5.5. Demonstration of photonics transitions (a) Spectrum of the drop port measured for a ring resonator with a radius of 100  $\mu\text{m}$ . A band-pass filter is used to eliminate amplified spontaneous emission noise of the input probe laser. The green line shows the reference spectrum when pump is off, and the probe beam is on one of the rings resonances. The red line shows the spectrum when the pump is on and demonstrates that the input light is transitioned to 15 of the ring resonators adjacent states (c) The diagram of the discrete cavity states of an optical microcavity before (b) and after (c) pump is incident on the sample. The diagram illustrates that light is transition from one state to many other states when the resonator is dynamically tuned. (from [86]) .....77

Figure 5.6. Cavities influence on photonic transitions a) Spectrum measured at the drop port of the ring resonator when the pump is off. The input wavelength of the CW laser is in resonance with the ring cavity (large peak). The smaller peaks are the other resonances of the ring resonator which are excited by the amplified spontaneous emission noise of the probe laser. b) Spectrum when the pump is turned on. However, the input probe wavelength is detuned from the rings resonance therefore no photonic transitions are evident. c) Same as in (b) but now the input wavelength is in resonance with the ring cavity. Seven new wavelengths appear in the spectrum. The black arrows indicate the original modes and the green arrows indicate the wavelengths generated by the photonic transitions. (from [86]) .....81

Figure 5.7. Changing the transition probabilities by increasing the cavity tuning. The spectrums for three different cavity tunings (increasing from top to bottom) are shown. It is seen that the amount of light in each of the final modes depends on the degree of cavity tuning (The amount of cavity tuning increases linearly with

pump energy). The spectrums are as follows: (top) Tuning: 0.66 nm, 0-order efficiency: 19%, 1<sup>st</sup>-order efficiency: 3.6% (middle) Tuning: 0.96 nm, 0-order efficiency: 7.5%, 1<sup>st</sup>-order efficiency: 3.7% (bottom) Tuning: 1.25 nm, 0-order efficiency: 3.3% 1<sup>st</sup>-order efficiency: 5%.....82

Figure 5.8. Spectra for different pump pulse durations. It is evident that the probability of nonadiabatic transitions increase as the pulse duration becomes shorter. (from [86]) .....83

# **CHAPTER 1**



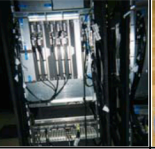

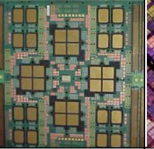
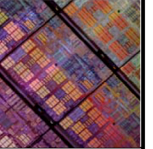
## **SILICON NANOPHOTONICS INTRODUCTION**

### **1.1 SILICON OPTICAL INTERCONNECTS**

Electronic devices are becoming faster and faster; however, over the last several decades, the electrical interconnections between these devices have had trouble keeping up [4]. For example, most long haul high-speed data/voice communications use fiber optic connections instead of an electrical option because the signal loss in electrical wires is too high [1]. On a shorter scale, the buses that carry information from one chip to another inside a computer system consistently run at much slower speeds than the chips themselves due to problems with electrical interconnects. The electronics industry expects that soon even the interconnections within the chips will not be fast enough to sustain the speeds of the individual transistors. Like the case for long haul telecommunications, replacing electrical interconnects with optical interconnects at ever-shorter scales offers an ideal solution because of the ability for optical interconnects to offer high bandwidths, low latencies, and low power operation [5]. IBM has outlined a timeline for such a transition to optical interconnects for the varying length scales as seen in Figure 1.1 [3]. Recently optical interconnects have become quite common at the inter-rack scale and even within the rack and there have already been significant commercial developments at the board and even at the chip level [6-8].

As the need for optical interconnects at smaller scales increases, the need for complex systems that integrate optical and electrical components arises. And the monolithic integration of a suite of optical and electronic capabilities on one substrate is the natural progression for the vision of such an integrated photonic system. Because of its widespread use in the very mature microelectronics industry, silicon is

the natural choice for such a platform [9]. Silicon, however, has not traditionally been considered an ideal optical material due to its low electro-optic coefficients, low light emission efficiency, and high fiber-to-waveguide coupling losses. However, silicon has several big advantages. It is transparent at telecommunication wavelengths, enabling the direct interfacing with fiber based telecommunication networks and equipment. Another advantage is that silicon has a high index of refraction (136% larger than Silica glass used for fibers), which enables very compact micron sized devices. Compact devices can operate with very low powers and are considerably more sensitive than their larger counterparts. In addition, recent progress in nanofabrication techniques and efficient fiber-waveguide couplers has rendered most of the previous problems obsolete (such as, weak non-linear effects and high losses), making silicon an excellent platform for the integration of complex electronic and photonic functionality all on one chip [10, 11].

	WAN	Inter-Rack	Rack	Server	Board	Chip
						
Length	Km	10-300m	1-10m	0.3-1m	0.1-0.3m	<20mm
Adoption	Since 80s	Since 90s	2-4 Years	5 Years	6-10 Years	10+ Years

**Figure 1.1.** Optical interconnect timeline for various length scales (from [3]).

## 1.2 PASSIVE SILICON NANOPHOTONIC DEVICES

So far many different passive silicon nanophotonic devices have been demonstrated. Such as, waveguide branches and sharp bends [12], ultra-high Q photonic crystal nanocavities [13, 14], ring resonators [15-18] and microdisc resonators [19]. However, the flow of light in all of these devices is fixed by the devices design and fabrication. The challenge is to achieve active silicon nanophotonic devices which are low-powered, ultra-fast and very compact.

## 1.3 SILICONS OPTICAL PROPERTIES FOR ACHIEVING ACTIVE DEVICES

In this dissertation I will focus on dynamic silicon nanophotonic devices on a chip. There are several mechanisms in silicon for achieving active devices. The first effect that we will consider, and also happens to be one of the strongest, is the thermo-optic effect where the refractive index of Silicon changes with temperature and is given by [20, 21]:

$$\frac{dn}{dT} = 1.86 \times 10^{-4} K^{-1} \quad (1.1)$$

However, this effect is quite slow, in turn, only allowing devices to operate at a maximum speed of approximately 1 MHz [20, 22].

Since silicon is centrosymmetric there is no Pockel's or any other  $\chi^2$  effects [23]. So, we turn our attention to the Franz-Keldysh and Kerr ( $\chi^3$ ) effects. The Franz-Keldysh effect is known as an electro-absorption effect because it changes the absorption of silicon when an external field is applied. The external field induces tunneling between the valence and conduction band. Since it is a band effect it is most prominent near the bandgap of Silicon at  $E_g=1.12$  eV, which is a serious disadvantage because this corresponds to a wavelength of approximately  $1.1 \mu m$ , which is not used in telecommunications systems. In addition, the Franz-Keldysh effect is quite small; it

induces a change in absorption of approximately  $2.5 \text{ cm}^{-1}$  at  $1.1 \text{ }\mu\text{m}$  and less than a  $10^{\text{th}}$  of that at telecom wavelengths [23], in turn, requiring centimeter long devices in order to get an appreciable change in transmission.

The Kerr effect in Silicon has been measured to have the following coefficients [24]:

$$n_2 = 0.45 \times 10^{-13} \left( \text{cm}^2/\text{W} \right) \quad (1.2)$$

$$\beta = 0.79 \left( \text{cm}/\text{GW} \right) \quad (1.3)$$

where  $n_2$  is the intensity dependent refractive index, and  $\beta$  is the two-photon absorption coefficient. Assuming typical silicon waveguide dimensions of  $450 \times 250 \text{ nm}$  and an average optical power of  $1 \text{ mW}$  we can calculate that  $n_2 = 4 \times 10^{-8}$  and  $\beta = 7 \times 10^{-4} \text{ cm}^{-1}$ . Obviously this effect is quite weak and in order to take advantage of it short pulses with peak powers of at least  $10 \text{ W}$  ( $1 \text{ pJ}$ ,  $100 \text{ fs}$  pulse) are needed. Such pulses are easily attainable but it is questionable whether they are telecommunications compatible and meet the goal of achieving low-powered devices.

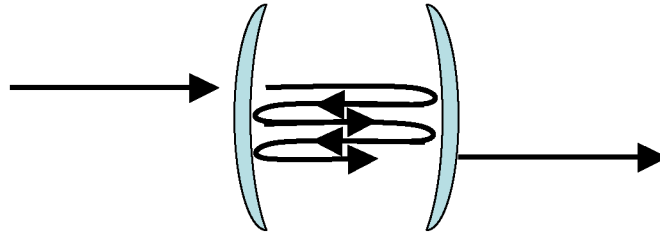
The last appreciable effect in Silicon is the free-carrier plasma dispersion effect. When free-carriers are generated it changes the refractive index and absorption of silicon, as given by [25]:

$$\begin{aligned} \Delta n &= - \left[ 8.8 \times 10^{-22} \cdot \Delta N + 8.5 \times 10^{-18} \cdot (\Delta P)^{0.8} \right] \\ \Delta \alpha &= 8.5 \cdot 10^{-18} \cdot \Delta N + 6.0 \times 10^{-18} \cdot \Delta P \end{aligned} \quad (1.4)$$

Where  $\Delta N \text{ (cm}^{-3}\text{)}$  is the change in electron concentration,  $\Delta P \text{ (cm}^{-3}\text{)}$  is the change in hole concentration,  $\Delta n$  is the change in refractive index and  $\Delta \alpha \text{ (cm}^{-1}\text{)}$  is the change in absorption coefficient. For a carrier concentration of  $10^{17}$  the change in index and absorption are  $\Delta n = 0.0004$  and  $\Delta \alpha = 1.45 \text{ cm}^{-1}$  ( $e^{-1}$  of  $6.9 \text{ mm}$ ). Unfortunately the change is so small that it would require a big device and high powers in order to accumulate a

large phase or transmission change. However, the effect can be quite fast – it is only limited by how fast carriers can be moved in and out of the device, which can be less than 10 ps [26, 27].

#### 1.4 RESONATOR: KEY TO ACTIVE DEVICES



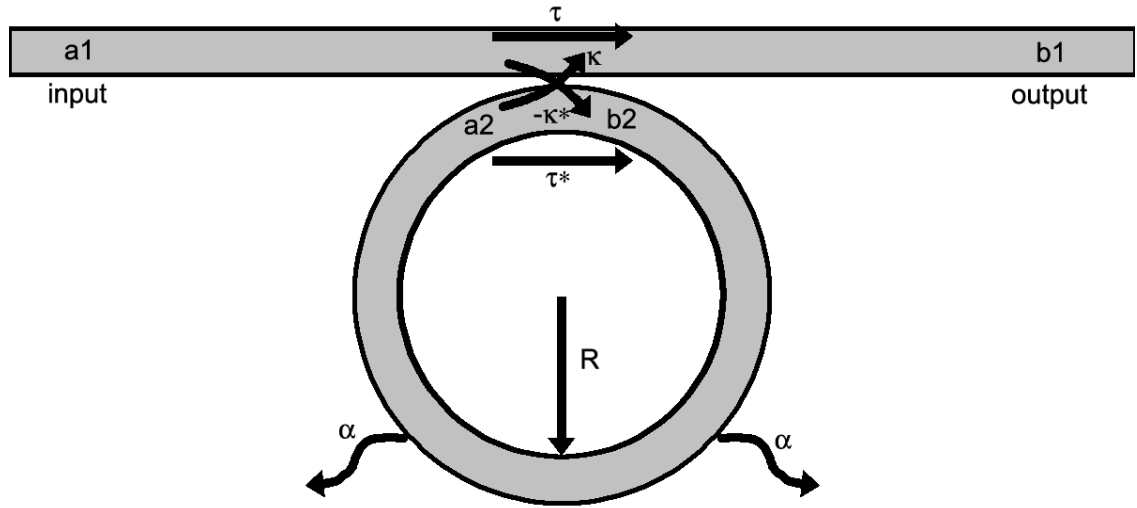
**Figure 1.2.** Schematic of a resonator showing that light traverses back and forth.

Even though the free-carrier plasma dispersion effect is quite weak we can exploit it by using a resonator to dramatically increase the sensitivity of the effect. Consider the schematic diagram of a resonator shown in Figure 1.2. The resonator is formed by two mirrors. And light is incident from the left, then bounces back and forth between the mirrors and finally exits after a certain number of bounces. Now imagine that the refractive index in the resonator has been changed by a small amount. After each pass the light will accumulate more and more of a phase change so that the total accumulated phase will be  $\Phi = N \cdot 2\pi/\lambda \cdot \Delta n \cdot d$  where  $N$  is the total number of passes,  $\lambda$  is the light's wavelength,  $\Delta n$  is the change in refractive index, and  $d$  is the mirror spacing. Therefore, we see that by using a resonator we can effectively accumulate the same amount of phase as in a device that is  $N$  times larger, where  $N$  can be anywhere from  $10^3$ - $10^6$  [13, 14, 28]. This point illustrates the advantage of using resonators in order to create a very compact device that operates with very low powers. The only tradeoff is that the resonator is highly wavelength sensitive. It can only transmit light when it is



on resonance, defined as when an integer multiple of wavelengths can fit between the two mirrors, and it becomes more and more sensitive to wavelength the higher the number of passes,  $N$ .

Now we will consider how a resonator works from a more theoretical framework based on coupled-mode theory. Since in this dissertation most of the work is done using ring resonators we will specifically derive the equations pertaining to it. However, similar expressions can be derived for the many other classes of resonators [29].



**Figure 1.3.** Schematic of a ring resonator

Consider the ring resonator schematic shown in Figure 1.3. It consists of lossless coupling between the input/output waveguide and the ring resonator, which can be described by the following matrix [30]:

$$\begin{bmatrix} b1 \\ b2 \end{bmatrix} = \begin{bmatrix} \tau & \kappa \\ -\kappa^* & \tau^* \end{bmatrix} \begin{bmatrix} a1 \\ a2 \end{bmatrix} \quad (1.5)$$

where  $\tau$  is the component of the amplitude that is not coupled, and  $\kappa$  is the waveguide-ring amplitude coupling coefficient. Since the coupling is lossless, by power conservation they are related by:

$$\tau^2 + \kappa^2 = 1 \quad (1.6)$$

In addition, the transmission around the ring resonator is given by:

$$a_2 = b_2 \cdot e^{-\alpha 2\pi R} \cdot e^{i 2\pi \frac{2\pi R}{\lambda_o} n_{eff}} \quad (1.7)$$

where  $\alpha$  is the propagation loss per unit length from scattering/absorption or any other processes (it could also be gain). From these equations we obtain that the power transmission of the ring resonator device is:

$$T = |b_1|^2 = \frac{\tau^2 + e^{-2\alpha 2\pi R} - 2\tau e^{-\alpha 2\pi R} \cos\left(2\pi \frac{2\pi R}{\lambda_o} n_{eff}\right)}{1 + \tau^2 e^{-2\alpha 2\pi R} - 2\tau e^{-\alpha 2\pi R} \cos\left(2\pi \frac{2\pi R}{\lambda_o} n_{eff}\right)} \quad (1.8)$$

And the total circulating power in the ring is:

$$C = |a_2|^2 = \frac{e^{-2\alpha 2\pi R} (1 - \tau^2)}{1 + \tau^2 e^{-2\alpha 2\pi R} - 2\tau e^{-\alpha 2\pi R} \cos\left(2\pi \frac{2\pi R}{\lambda_o} n_{eff}\right)} \quad (1.9)$$

On resonance (i.e. when  $2\pi R/\lambda_o n_{eff}$  is an integer) we get:

$$T = |b_1|^2 = \frac{(e^{-\alpha 2\pi R} - \tau)^2}{(1 - \tau e^{-\alpha 2\pi R})^2} \quad (1.10)$$

$$C = |a_2|^2 = \frac{e^{-2\alpha 2\pi R} (1 - \tau^2)}{(1 - \tau e^{-\alpha 2\pi R})^2} \quad (1.11)$$

From this we see that the transmission of the resonator can be 0, and the power circulating in the resonator is maximized when:

$$e^{-\alpha 2\pi R} = \tau \quad (1.12)$$

This condition is known as critical coupling and results from the perfect destructive interference of the transmitted field  $\tau a_1$  and the field coupled from the resonator  $\kappa a_2$ . Next it can be shown that the quality factor, which is the measure of the wavelength sensitivity of the resonator, is approximately given by [31]:

$$Q \equiv \frac{\lambda_o}{\Delta\lambda_{FWHM}} \approx \frac{\pi \sqrt{\tau e^{-\alpha 2\pi R}} 2\pi R n_g}{(1 - \tau e^{-\alpha 2\pi R}) \lambda_o} \quad (1.13)$$

where  $\Delta\lambda_{FWHM}$  is the Full-Width-Half-Maximum bandwidth of the resonance and  $n_g$  is the group index of the ring waveguide. We see from this result the verification that by either reducing the loss or by reducing the coupling to the waveguide (i.e. increasing  $\tau$ ) that the wavelength sensitivity (the  $Q$ ) increases. Reducing the loss/coupling is equivalent to increasing the number of round trips the light takes in the resonator. In addition, we see that the intensity in the resonator under critical coupling can be approximated from 1.11 as:

$$C = |a_2|^2 \approx \frac{1}{\alpha 2\pi R} \quad (1.14)$$

And we see that as the loss is reduced in the resonator (or as the coupling is reduced) the intensity in the ring resonator can dramatically increase because the light takes many more round trips in a very compact volume.

## 1.5 SUMMARY

In conclusion, we've shown the promise of using silicon nanophotonics for chip scale interconnects. We discussed the challenges associated with silicon, including the weak optical properties of the material. And proposed a solution where we use optical resonators to dramatically enhance the sensitivity to silicon's optical

properties. This enables us to realize active devices that are compact, fast and efficient. In the remainder of the dissertation we will present several novel active silicon nanophotonic devices that can be used in the silicon nanophotonics toolset. In Chapter 3 we also discuss how to design more efficient devices using evolutionary algorithms.

## CHAPTER 2

### ALL-OPTICAL SWITCHING AND MODULATION

#### 2.1 INTRODUCTION

One of the most basic functionalities of an active silicon nanophotonic chip is the ability to switch, route and/or modulate a beam of light. In general, there are three mechanisms for changing the flow of light in silicon – optically, electrically and thermally. As discussed in chapter 1.3 the thermo-optic effect in Silicon is large, however, even with the most recent designs switching speeds are limited to approximately 100 kHz to 1 MHz [20, 32]. Optical effects, such as the Kerr effect, are generally negligible for only but the highest pump powers making such an effect incompatible with a realistic on-chip platform [33]. The only other fast effect that is appreciably significant is the free-carrier plasma dispersion effect, which can be invoked either electrically or optically through linear or non-linear absorption. However, up until only recently, this effect required very large devices and high powers in order to significantly accumulate enough phase or intensity change [16, 17].

Almeida and Barrios showed that by using a resonator it is possible to significantly increase the sensitivity of the free-carrier plasma-dispersion effect, in turn, enabling compact and ultra-low powered all-optical (and electro-optic) switching and modulation [16, 17, 34]. They demonstrated that using a 10  $\mu\text{m}$  ring resonator it is possible to modulate a beam of light using less than 1 pJ of pump beam energy, with modulation depths greater than 70%, and with switching times of 450 ps. Although this is a significant improvement over previous devices there are several improvements that can be made in order to obtain better performance.

The first issue that I will address in this chapter is the required pump energy. It is well known that the energy needed to shift the resonance of a resonator is

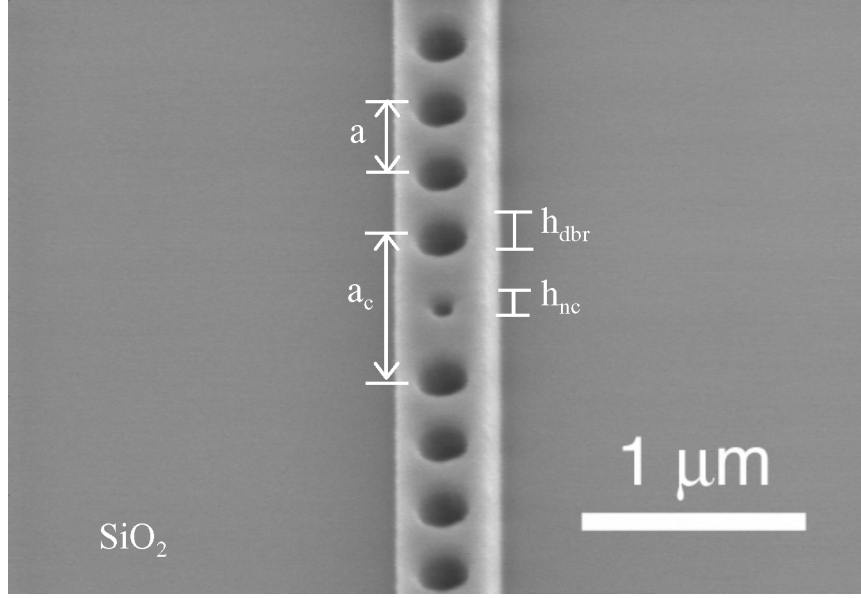
proportional to  $E_{\text{switch}} \propto V/Q$ , where  $V$  is the mode volume and  $Q$  is the quality factor of the resonator [35]. Given a fixed quality factor, it is relatively intuitive that by reducing the size of the device the required switching energy will correspondingly decrease. Here I will show this is the case by demonstrating all-optical switching in a photonic crystal device with a mode volume of only  $V=0.1 \mu\text{m}^3$ , compared to the ring resonators mode volume of approximately  $7 \mu\text{m}^3$ . This work was the first demonstration of an all-optical switch using a photonic crystal device in *any* material system, in turn, highlighting the promise of using photonic crystals for achieving ultra-compact low-powered devices.

Next I will address the issue of the switching speed of the device. In Almeida's previous device the speed was limited to approximately 450 ps, which was determined by the recombination of the photo-excited free-carriers. The bulk recombination lifetime of Silicon is on the order of microseconds. In Almeida's ring resonator device the recombination is primarily determined by surface-states introduced by the etching of the Silicon waveguides during the fabrication process. One approach to increase the speed of the device is by introducing more defect states through either more surface etching or by ion-implantation [16, 17]. However, both of these approaches have a severe drawback in that they will introduce additional loss, which will significantly affect the Quality Factor of the ring resonator, and consequently increase the required switching energy. Instead, the approach I used to significantly increase the speed of the device is to introduce a PIN-diode around the ring resonator and use it to quickly extract the free carriers using the electric field of the reverse biased diode. With this device I will show an order of magnitude increase in switching speed, enabling 20+ GHz all-optical modulation/switching on a chip.

## 2.2 PHOTONIC CRYSTAL DEVICE

Figure 2.1 shows a scanning electron micrograph of the photonic crystal device used to demonstrate all-optical switching. The one-dimensional photonic crystal (see [36]) consists of a high index contrast Silicon waveguide (width 450 nm, height 250 nm) embedded with two sets of four silicon dioxide ( $\text{SiO}_2$ ) filled holes of diameter  $h_{\text{dbr}}$  (200 nm). The set of four holes are spaced apart by  $a$  (380 nm), creating a distributed bragg reflector (DBR). The two sets of DBRs are spaced apart by  $a_c$  (880 nm), forming a nanosized cavity where the field is greatly enhanced, in turn, increasing the devices sensitivity to small refractive index changes. A small 100 nm ( $h_{\text{nc}}$ ) diameter  $\text{SiO}_2$  filled hole is embedded in the center of the nano-cavity. The addition of this defect at the center of the cavity creates a local discontinuity in the field, increasing the strength of the field in the center of the cavity, which improves the sensitivity of the device [37]. The devices were fabricated using Silicon on Insulator (SOI) wafers with 250 nm of crystalline silicon on top of a three microns thick buried oxide layer. The structure was defined using electron-beam lithography using FOx-12 spin-on oxide as a negative resist and etch mask and etched by Chlorine based reactive ion etching (RIE). The holes were filled and the structure clad with  $\text{SiO}_2$  using plasma enhanced chemical vapor deposition.

The measured transmission of the quasi-TE (electric field parallel to the plane of the chip) mode of the device, as shown in Figure 2.2, is highly wavelength dependent. Due to the resonant nature of the nano-cavity, only light with a wavelength



**Figure 2.1.** Scanning electron micrograph of the top-view of an one-dimensional photonic crystal nanocavity embedded in a Silicon waveguide (from [38]).

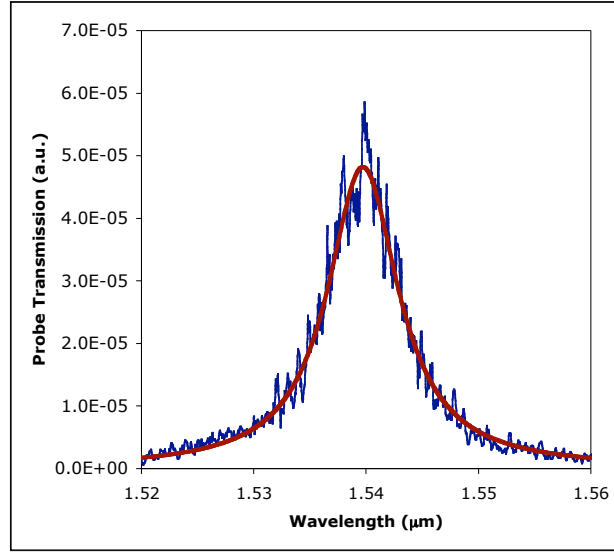
that is a half-integer multiple of the effective cavity length is efficiently transmitted. The device transmission can be modeled by assuming that it is equivalent to a Fabry-Perot cavity given by

$$T = \frac{I_{out}}{I_{in}} = \frac{L(1-R)^2}{(1-LR)^2 + 4LR \sin^2\left(\frac{2\pi}{\lambda} n_{eff} d\right)} S \quad (2.1)$$

where  $S$  is a scaling factor,  $L$  are the round-trip losses of the cavity,  $R$  is the reflectivity of the distributed Bragg reflectors,  $n_{eff}$  is the effective index of the waveguide,  $d$  is the effective cavity length, and  $\lambda$  is the wavelength of the probe light [16]. The model was fitted, as shown in Figure 2.2, to the measured transmission using:  $S = 4.8196e-5$ ,  $L = 1$  (assumed lossless),  $R = 0.9542$ ,  $n_{eff} = 2.46$  (calculated using an eigenmode solver), and  $d = 0.939 \mu m$  ( $\approx 3(\lambda_r/2n_{eff})$ ). The cavity quality-factor is  $Q = \lambda_r / \Delta\lambda_{FWHM} = (2\pi n_{eff} d / \lambda_r) (R^{0.5} / (1-R)) = 200$ , where  $\lambda_r = 1.54 \mu m$  is the



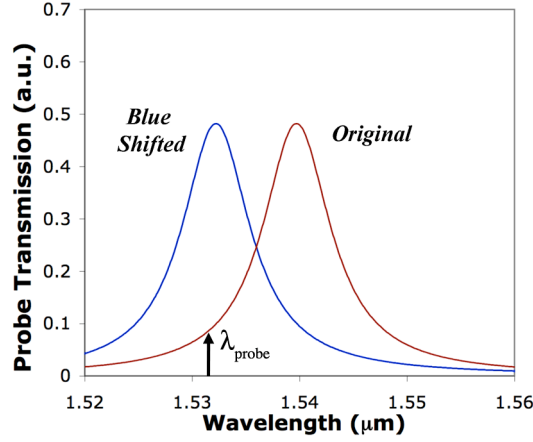
resonance wavelength, and  $\Delta\lambda_{FWHM} = 7.7$  nm is the resonance full-width-at-half-maximum (FWHM). This quality factor corresponds to a cavity photon lifetime of  $\lambda_r^2/(2\pi c\Delta\lambda_{FWHM}) = 0.165$  ps, where  $c$  is the speed of light in vacuum [16]. This relatively short cavity lifetime corresponds to the lower limit for the temporal response of a device based on such a cavity.



**Figure 2.2.** Measured and fitted transmission of the one-dimensional photonic crystal nano-cavity device (from [38]).

Due to the high confinement nature of the photonic crystal device, a small refractive index change in the cavity leads to a large shift of the resonators spectrum. Consequently, a probe signal operating at a wavelength close to the resonators spectrum can be strongly modulated. As seen in Figure 2.3, by blue-shifting the resonators spectrum by 8 nm, a probe signal fixed at  $\lambda_{\text{probe}} = 1532$  nm, can be modulated from “OFF” (original spectrum) to “ON” (shifted spectrum). As will be shown later, an 8nm shift is possible with a refractive index change as small as 0.025.

This shifting of the cavity spectrum is the basic means used to achieve all-optical switching.

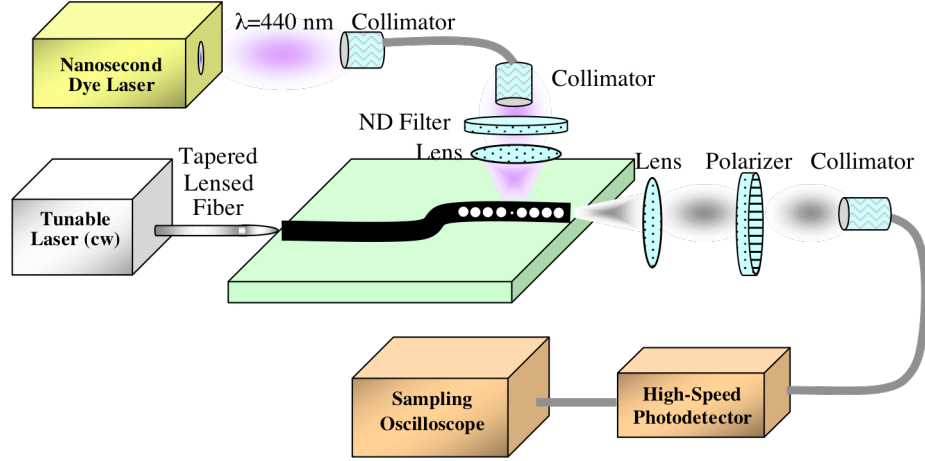


**Figure 2.3.** Example probe transmission before and after an 8 nm blue-shift of the cavity spectrum, demonstrating that a probe signal with a fixed wavelength ( $\lambda_{\text{probe}}=1.532$  nm in this example) can be modulated from off to on (from [38]).

### 2.2.1 SLOW SWITCHING

Here we use nanosecond pump pulses centered at a wavelength  $\lambda_{\text{pump}} = 440$  nm to inject free-carriers within the one-dimensional photonic crystal cavity and thereby tune its real refractive index and optical absorption coefficient. At this wavelength, the strong linear absorption in silicon causes 90% of the photons transmitted into the top-silicon layer to be absorbed within a thickness of only 250 nm. Once the pulse is absorbed, photo-excited free-carrier electron-hole pairs are generated inside the photonic crystal, inducing a change in the real refractive index and optical absorption coefficient, as given by [25]:

$$\begin{aligned}\Delta n &= -\left[8.8 \times 10^{-22} \cdot \Delta N + 8.5 \times 10^{-18} \cdot (\Delta P)^{0.8}\right] \\ \Delta \alpha &= 8.5 \times 10^{-18} \cdot \Delta N + 6.0 \times 10^{-18} \cdot \Delta P\end{aligned}\tag{2.2}$$



**Figure 2.4.** Schematic of the pump-and-probe setup. A nanosecond dye laser is used to pump the device. A tunable laser is used to probe the device. Probe light transmitted thru the device is collected at the output of the waveguide and fed into a high-speed photodetector (from [38]).

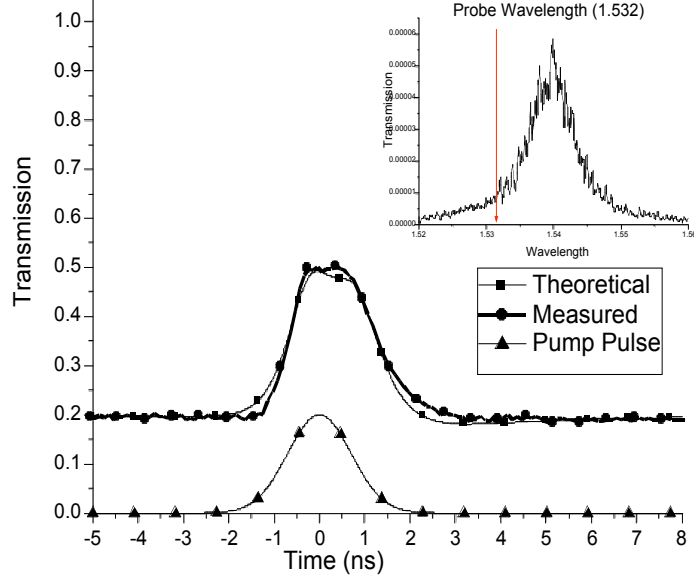
where  $\Delta n$  is the real refractive index change,  $\Delta\alpha$  is the absorption coefficient change (in  $\text{cm}^{-1}$ ),  $\Delta N$  is the change in the electron concentration (in  $\text{cm}^{-3}$ ), and  $\Delta P$  is the change in the hole concentration (in  $\text{cm}^{-3}$ ). The change in the cavities refractive index causes the spectrum to blue-shift as seen in Figure 2.3.

Figure 2.4 shows the schematic of the pump-and-probe setup used for characterizing the device. The laser source for the pump is a dye laser pumped by a Q-switched Nitrogen laser. The dye (Coumarin 440) laser generates 2.4 ns pulses at  $\lambda_{\text{pump}} = 440\text{ nm}$  with nano-Joule pulse energies at a 36.5 Hz repetition rate. The pump light is coupled into a single mode fiber. The output from the fiber is collimated and then attenuated using neutral density filters before being focused by a lens onto a spot diameter of  $3\text{ }\mu\text{m}$  centered on the device, completely covering the nano-cavity and the DBR's. A tunable continuous-wave laser provides the probe signal at wavelength  $\lambda_{\text{probe}}$  which is coupled into the silicon waveguide by an external tapered-lensed fiber

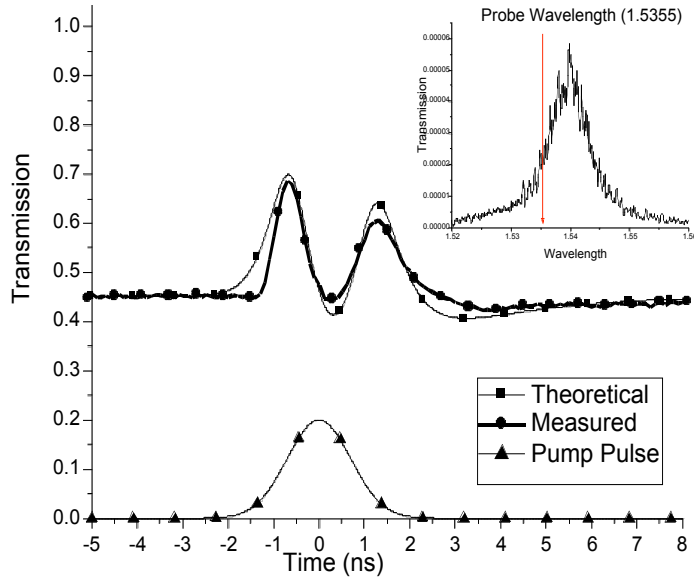
and an on-chip fiber-to-waveguide nanotaper coupler [10]. The quasi-TE transmitted light is collimated by a lens ( $NA = 0.55$ ), discriminated by a polarizer, and focused into single mode fiber through a collimator. The probe signal is detected by a high-speed DC-33GHz photodetector with a nominal fall/rise time of 30 ps and 650 Volt/Watt gain. A 20-GHz digital sampling oscilloscope is used to record the probe signal.

The temporal response of the transmitted probe signals are shown in Figure 2.5-2.7 for three probe wavelengths  $\lambda_{\text{probe}} = 1532$  nm (below resonance),  $\lambda_{\text{probe}} = 1535.5$  nm (half-width-at-half-maximum [HWHM] below resonance), and  $\lambda_{\text{probe}} = 1539.5$  nm (on resonance), respectively. The pulse energy incident on the device plane is approximately 60pJ. These temporal responses confirm that the free-carrier plasma dispersion effect (FCPDE) is the dominant mechanism for inducing the modulation of the probe signal. Figure 2.5 and Figure 2.6 show that the transmitted probe power increases when the pump is incident on the device. This increase is due to a blue shift of the spectrum, induced by a reduction of the real refractive index in Silicon from the generation of free-carriers.

In Figure 2.6 the probe wavelength is set a HWHM below the resonance. Under optical pumping, once the resonance is fully shifted, the probe wavelength is *effectively* a HWHM above the resonance (it's actually only shifted to the 70% point but the probes transmission is reduced by strong optical absorption at the peak of the pump pulse). Thus, the transmitted probe power increases then decreases on the rise of the pump pulse, and then increases and decreases again on the fall of the pump pulse. From this we can ascertain that the maximum response time of the device is definitely less than 1.5ns (a fall-rise cycle).

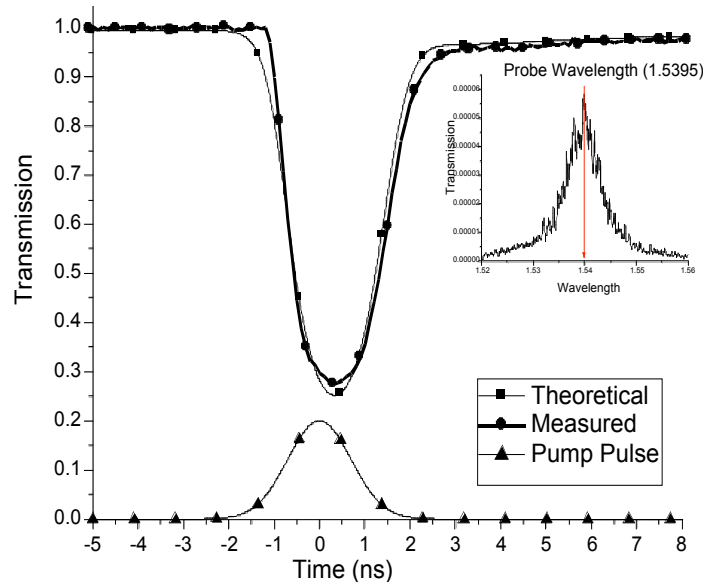


**Figure 2.5.** Temporal response of probe at  $\lambda_{\text{probe}} = 1532$  nm (below resonance). The pump is not to scale and is only for reference (from [38]).



**Figure 2.6.** Temporal response of probe at  $\lambda_{\text{probe}} = 1535.5$  nm (Half-width-at-half-maximum below resonance). The pump is not to scale and is only for reference (from [38]).

The modulation depth, defined as  $MD = (I_{max} - I_{min}) / I_{max}$ , where  $I_{max}$  and  $I_{min}$  are, respectively, the maximum and minimum transmitted probe optical power, was measured to be  $MD = 60\%$  for  $\lambda_{probe} = 1532$  nm (Figure 2.5) and  $MD = 71\%$  for  $\lambda_{probe} = 1539.5$  nm (Figure 2.7). The modulation depth is limited by optical absorption induced by an increased concentration of free carriers. The modulation depth can be improved by using a photonic crystal nano-cavity with a higher quality factor, consequently requiring fewer free-carriers to induce a smaller spectrum shift.



**Figure 2.7.** Temporal response of probe at  $\lambda_{probe} = 1539.5$  nm (on resonance). The pump is not to scale and is only for reference (from [38]).

From these results it is seen that there is a small thermal contribution to the temporal response of the probe. The thermooptic effect induces a change in the real refractive index of Silicon as given by [21]:

$$\Delta n = 1.8 \times 10^{-4} \cdot \Delta T \quad (2.3)$$

where  $\Delta T$  (in Kelvin) is the induced change in temperature. The refractive index change results in a red-shift of the cavity spectrum. The effect is seen in Figure 2.7 for

the case where the probe wavelength is set to the resonance wavelength. One can see that following the pump pulse, the transmitted probe power recovers to 100% only after several nanoseconds. This is because the induced red-shift of the cavity spectrum keeps the device slightly off-resonance until the heat has sufficiently diffused.

The thermo-optic effect is also clear in Figure 2.6 where the second maximum (i.e. on the decline of the pump pulse) does not quite reach the same level as the first. This is because the free-carrier plasma dispersion effect and the thermo-optic effect are competing processes (i.e. blue-shift vs. red-shift). At the beginning of the pulse the FCPDE dominates but at the end the thermo-optic effect is “prematurely” recovering the cavity spectrum towards its original position, however, the optical absorption induced by the free-carriers is still significant, in turn reducing the level of the second maximum. If the thermal effect were absent both of the peaks should be exactly the same.

The theoretical temporal response of the probe signal was obtained by modeling the free carrier dynamics and the thermal effects. The free-carriers are subject to the rate equation given by [39]

$$\begin{aligned} \frac{d\Delta N}{dt} &= -\frac{\Delta N}{\tau_{fc}} + R_{pump}(t) \\ R_{pump}(t) &= N_{ph} e^{\left(-t/\tau_{pump}\right)^2} \end{aligned} \quad (2.4)$$

where  $\Delta N = \Delta P$  is the change in free carrier concentration,  $\tau_{fc}$  is the free-carrier lifetime,  $R_{pump}$  is the pumping rate,  $N_{ph}$  is the number of photons absorbed by the device, and  $\tau_{pump}$  is the duration of the pump pulse. The first term of Eq. 2.4 models the relaxation of the free-carriers from their excited state and is dictated by the free-carrier lifetime. The second term is the excitation of the free-carriers after absorbing a pump photon.

When free-carriers are generated by the 400nm pump beam there is excess energy with respect to the bandgap of Silicon. This excess energy is quickly converted to thermal energy ( $E_{\text{pump}} - E_{\text{bandgap}}$ ), following the relaxation from the initial energy level ( $E_{\text{pump}}$ ) to the bottom of the conduction band. Additional heat is then generated from multi-phonon processes that relax the free-carriers from the conduction band to the valence band. Heat generated from Auger recombination is negligible because with the induced carrier concentration ( $\sim 10^{19} \text{ cm}^{-3}$ ) in this device the Auger lifetime is greater than 10ns [40], considerably longer than the free-carrier lifetime. Thus, the change in the thermal energy is subject to the rate equation given by [39]

$$\begin{aligned} \frac{d\Delta Q}{dt} &= (E_{\text{pump}} - E_{\text{bandgap}}) \cdot R_{\text{pump}}(t) + E_{\text{bandgap}} \cdot \frac{\Delta N}{\tau_{\text{fc}}} - \frac{\Delta Q}{\tau_{\text{tr}}} \\ \Delta T &= \frac{\Delta Q}{\rho_{\text{Si}} C_v} \end{aligned} \quad (2.5)$$

where  $\Delta Q$  is the change in thermal energy per unit volume,  $E_{\text{pump}}$  is the energy of a pump photon ( $\lambda_{\text{pump}}=440 \text{ nm}$ ),  $E_{\text{bandgap}}$  is the bandgap of Silicon,  $\tau_{\text{tr}}$  is the thermal relaxation time,  $\Delta T$  is the change in temperature,  $\rho_{\text{Si}} = 2.33 \cdot 10^{-3} \text{ (in kg/cm}^3\text{)}$  is the density of Silicon, and  $C_v = 705 \text{ (in J/(kg-K))}$  is the heat capacity of Silicon. The first term of Eq. 2.5 models the instantaneous heat generation from excess photon energy, the second term models the generation of additional thermal energy from multi-phonon relaxation processes, and the last term models the relaxation of the additional thermal energy from heat diffusion.

The theoretical temporal response of the probe signal was obtained by applying the pump excitation ( $R_{\text{pump}}(t)$ ) to the above rate equations (Eq. 2.4 and 2.5). The generation of free-carriers ( $\Delta N = \Delta P$ ) induces a change in refractive index and optical absorption given by Eq. 2.2. The temperature change induces a refractive index

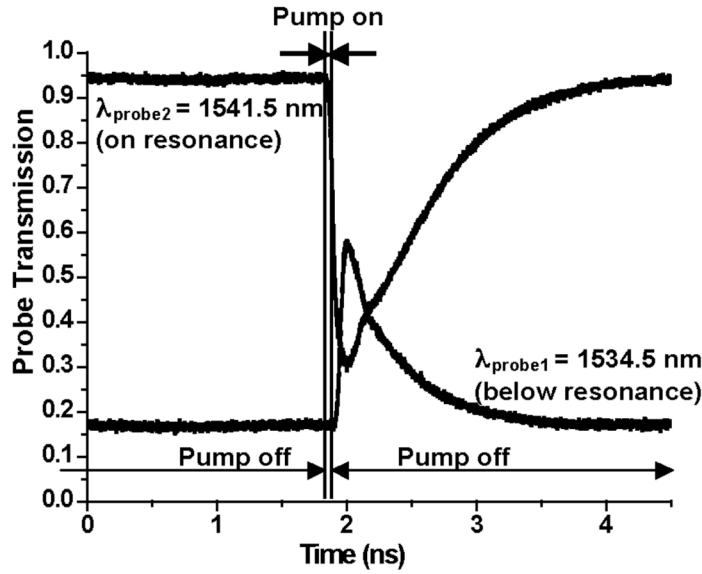


change given by Eq. 2.3. Applying these changes of the refractive index and optical absorption to the cavity spectrum fit from Eq. 2.1, at a fixed probe wavelength, the temporal response of the cavity transmission can be obtained. Since the pump excitation was applied to not just the nano-cavity, but also the DBRs, three-dimensional finite-difference-time-domain simulations were used in conjunction with Eq. 1 to obtain the change in the cavity spectrum from the changes of real refractive index and optical absorption coefficient. It was found that an  $\Delta n = -0.02$  refractive index change induces a  $\Delta\lambda = -6.4$  nm shift in the cavity spectrum and that the variation is linear. The cavity losses from absorption,  $L = \exp(-\Delta\alpha d_{RT})$  (from Eq. 1), were obtained using  $d_{RT} = 1.2$   $\mu\text{m}$ , where  $d_{RT}$  is the effective round-trip cavity length.

We obtain from the experimental data and the theoretical model that the maximum wavelength shift of the cavity spectrum is  $\Delta\lambda = -6.7$  nm. This corresponds to a total refractive index change in the silicon of  $\Delta n = -0.021$ . The refractive index change attributed to the free-carrier plasma dispersion effect is  $\Delta n = -0.025$ . This refractive index change is caused by an equivalent free-carrier concentration of  $\Delta N = \Delta P = 1.14 \cdot 10^{19} \text{ cm}^{-3}$ . This concentration induces an optical absorption coefficient of  $\Delta\alpha = 0.0165 \text{ } \mu\text{m}^{-1}$  (0.07 dB/ $\mu\text{m}$ ). We also determined that the thermo-optically induced refractive index change is  $\Delta n = +0.004$ . This refractive index change is 6.5 times smaller than the one from the FCPDE effect, confirming the dominance of the FCPDE as the primary modulation mechanism. Considering the pump beam size and profile, the overlap of the beam with the geometry of the device, and the reflections from the focusing lens and the interfaces in the structure, we estimate that the device absorbed only 7 pJ of the incident 60 pJ of pump energy.

### 2.2.2 FAST SWITCHING

In the previous section nanosecond pump pulses were used. Here we use a much shorter pump pulse in order to determine the maximum speed of this device and the performance relative to Almeida's ring resonator device. The experimental setup is similar to the one seen in Figure 2.4 except the pump source is now a Ti:Sapphire laser that has been frequency doubled to 415 nm using a BBO (Beta-Barium Borate) crystal. The pulses have a duration of 1.5 ps.



**Figure 2.8.** Temporal response of a probe signal for two different probe wavelengths (on resonance and below resonance) using a one-dimensional photonic crystal nanocavity (from [41]).

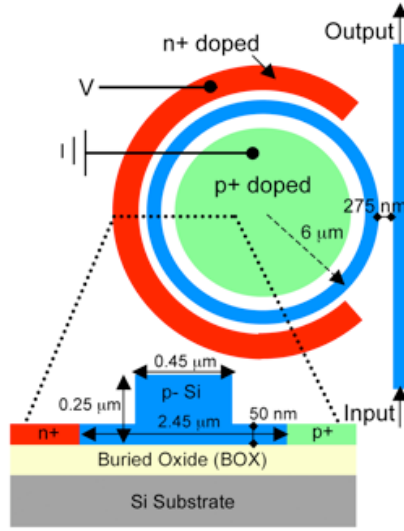
The temporal response of the transmitted probe signals are shown in Figure 2.8 for two probe wavelengths:  $\lambda_{\text{probe1}} = 1,534.5 \text{ nm}$  (below resonance) and  $\lambda_{\text{probe2}} = 1,541.5 \text{ nm}$  (on resonance). The probe signals were both modulated by 70%. We obtained from the experimental data a wavelength peak shift of  $\Delta\lambda = -4.5 \text{ nm}$  and a relaxation time of  $\tau_{fc} = 470 \text{ ps}$ . Taking all reflections from the different interfaces and

the size of the focused pump beam into account, we estimate that only 1 pJ of linearly absorbed pulse energy was needed to achieve this modulation. Therefore, the one-dimensional photonic crystal nanocavity achieved a  $\sim 12.5$  larger wavelength peak shift with only  $\sim 6.7$  times more pulse energy than the ring resonator modulator [16, 17]. The amount of wavelength shift can be considerably reduced, and also the pulse energy, by using a high quality factor two-dimensional photonic crystal nanocavity as a modulator.

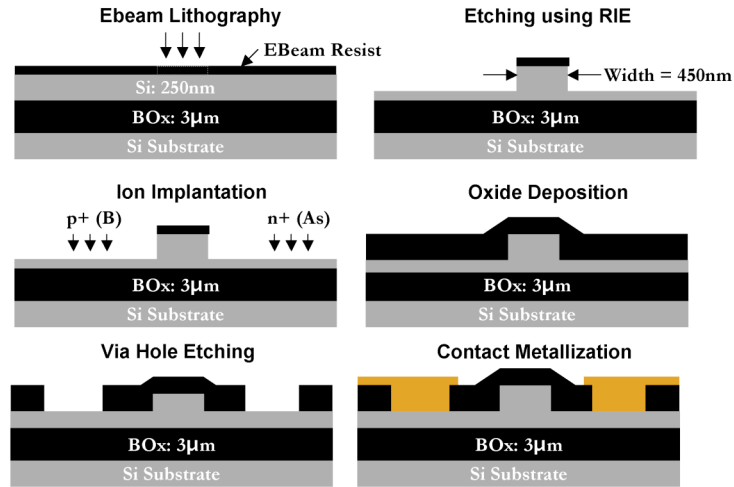
### 2.3 ULTRA-FAST SWITCHING USING AN INTEGRATED DIODE

In previous experiments the modulation time of the device was limited to 450 ps by the carrier recombination time dictated by the unpassivated sidewalls of the structures. In contrast, here we demonstrate all optical modulation with picosecond modulation time by incorporating a p-i-n diode into the ring resonator device. The effective free-carrier lifetime of photo-excited carriers can be greatly reduced by reverse biasing this diode [42, 43]. The applied voltage induces an electric field across the intrinsic region where the waveguide lies, enabling the extraction of the generated electron-hole pairs from the waveguide under reverse bias.

A schematic drawing and the fabrication details of the p-i-n diode ring resonator device can be seen in Figure 2.9 and Figure 2.10. The diode is formed around the ring resonator waveguide. It is well known that a ring resonator, coupled to a waveguide, has an optical transmission that is highly sensitive to signal wavelength and is greatly reduced at wavelengths in which the rings circumference



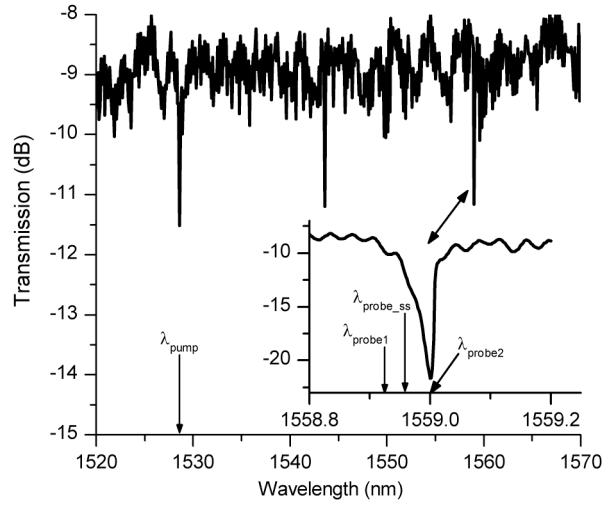
**Figure 2.9.** Schematic drawing of the PIN ring resonator device used for all-optical modulation. A reverse bias is applied across the ring in order to extract carriers quickly.



**Figure 2.10.** PIN diode ring resonator fabrication process. All of the masks are defined using electron-beam lithography.

corresponds to an integer multiple of guided wavelengths. By tuning the refractive index of the ring waveguide, the resonant wavelengths of the device can be altered.

The measured passive spectrum of the device is seen in Figure 2.11. Here we use 10-ps pump pulses with a wavelength of  $\lambda_{\text{pump}} = 1528.6$  nm, close to one of the ring resonances, to inject free-carriers through two-photon absorption inside the ring resonator[16], thus inducing a change in the refractive index in the ring waveguide[25]. A continuous-wave probe beam with a wavelength close to another resonance will be strongly modulated by this induced



**Figure 2.11.** Passive measurement of the spectrum of the PIN ring resonator device.  $\lambda_{\text{pump}}$  is wavelength at which the pump beam operates and is tuned to one of the rings resonances. The inset shows the probe resonance where several probe wavelengths are indicated and are referred to.

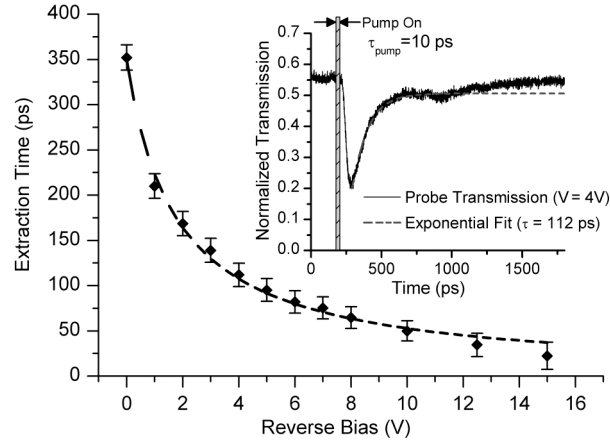
refractive index change. The probe beam wavelength is set around a resonance at  $\lambda_{\text{probe}} = 1559.0$  nm, corresponding to two free-spectral ranges ( $\text{FSR} = 15.2$  nm) away from the pump resonance. The transmission of the device is reduced by more than 13-dB at the probes resonance. The cavity quality-factors for the pump and probe resonances are  $Q_{\text{pump}} \approx \lambda_{\text{pump}} / \Delta\lambda_{\text{FWHMpu}} = 18200$  and  $Q_{\text{probe}} \approx \lambda_{\text{probe}} / \Delta\lambda_{\text{FWHMpr}} =$

39000 , where  $\Delta\lambda_{\text{FWHMpump}} = 0.084$  nm and  $\Delta\lambda_{\text{FWHMprobe}} = 0.04$  nm are the full-width-at-half-maximum bandwidths.

In order to dramatically increase the speed of the device the photo-excited free-carriers are extracted using a reverse-biased diode. To measure the extraction time the probe signal wavelength ( $\lambda_{\text{probe\_ss}} = 1558.973$ ) and pump energy coupled to the chip (8 pJ) are set so that probe wavelength is tuned only within the quasi-linear spectral region of the probe resonance (i.e. a small signal modulation) as is seen in Figure 2.11. This ensures that the extraction time can be directly measured from the probes dynamic time response. If the modulation were non-linear it would be more difficult to get this information from the data. We should note that the theoretical maximum modulation speed of this device, if the extraction time can be absolutely minimized, is fundamentally limited by the resonant cavity lifetimes as calculated to be  $\tau_{\text{pump}} = 14.8$  ps and  $\tau_{\text{probe}} = 32.3$  ps [16, 17].

Here we use the optical experimental setup described in [16]. The DC reverse-bias is applied to the ring resonator device using electrical probes. Figure 2.12 shows the measured extraction time as a function of reverse-bias voltage with errors bars derived from the uncertainty due to photo detector response time and cavity lifetime. The inset of Figure 2.12 shows the probe signal for a reverse bias voltage of 4V. As seen, the probe signal initially decreases after the pump pulse is applied. The time it takes for this transition to occur is determined by the resonant cavity lifetimes,  $\tau_{\text{probe}}$  and  $\tau_{\text{pump}}$ , which dictates how quickly the optical field in the resonator is built up. The initial decrease is then followed by an exponential increase, corresponding to the extraction time of the photo-excited carriers as determined by fitting a simple exponential decay to this part of the probe signal temporal response (shown as a dashed line over the temporal signal). After the exponential increase, the probe signal

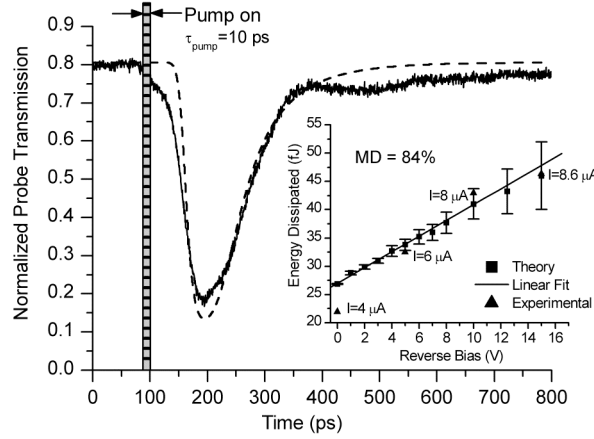
does not return to its initial state, but instead slowly increases, as a fraction of the carriers generated in the ring are not extracted by the diode because it only encompasses two-thirds of the ring as is seen in Figure 2.9. The dynamics of any carriers in the remaining third is solely determined by slow recombination mechanisms, and is thus equivalent to the open-circuit recombination time of 1.19 ns. If the diode were to encompass the entire ring then the carrier dynamics would solely be determined by the reverse-biased diode carrier extraction time.



**Figure 2.12.** Carrier extraction time as a function of reverse-bias voltage. The inset shows the temporal probe signal for reverse-bias  $V = 4\text{V}$  and the exponential fit used to obtain the extraction time ( $1/e$  point) (from [26]).

In order to investigate the performance of the device with large modulations the probe wavelength was set to  $\lambda_{\text{probe1}} = 1558.95\text{ nm}$ , the pump pulse energy coupled to the chip set to 19 pJ, and a reverse-bias voltage set to 10 V (extraction time 50 ps). Figure 2.13 shows the time dependence of the probe signal under these conditions. The amount of modulation, defined by  $\text{MD} = (I_{\text{max}} - I_{\text{min}})/I_{\text{max}}$ , where  $I_{\text{max}}$  and  $I_{\text{min}}$  are the maximum and minimum transmitted probe powers, is measured to be  $\text{MD}_{\text{probe}} =$

79.5%. This modulation depth (MD) is limited by the photodetector response time; the actual amount of modulation is estimated to be 84%. The time it takes for the probe signal to restore to its maximum value from the minimum of its transmission is measured to be  $\tau = 122$  ps. This time is longer than the extraction time (50 ps)



**Figure 2.13.** Experimental (solid) and theoretical (dashed) temporal response of the probe signal with reverse-bias  $V = 10$  V. The inset shows the required switching energy (Pump Energy Dissipated) needed to maintain the same modulation depth for different reverse biases (from [26]).

because the time response of the device is determined by the convolution of the free-carrier dynamics (an exponential decay of 50 ps) and the non-linear modulated spectrum (a lorentzian), at this pump energy and probe wavelength. Another contributing factor is the third of the ring waveguide where the carriers cannot be extracted. This region has a stronger contribution here because the larger pump energy injects more free-carriers, which take more time to recombine to a small enough level to change the probes transmission. In turn, the slowly recombining carriers act to slow the return of the probe transmission to its maximum value.



The theoretical time dependence of the probe signal transmission shown in Figure 2.13 (dashed-line) is calculated using an analytical model for the ring resonator transmission [30], and a model of the carrier dynamics governed by the following rate equations:

$$\begin{aligned}\frac{d\Delta N}{dt} &= -\frac{2}{3} \cdot \frac{\Delta N}{\tau_{\text{extract}}} - \frac{1}{3} \cdot \frac{\Delta N}{\tau_{\text{open}}} + \frac{n}{\tau_{\text{probe}}} \\ \frac{dn}{dt} &= -\frac{n}{\tau_{\text{probe}}} + \frac{N_{\text{ph}}}{2 \cdot (\tau_{\text{pump}}/2) \cdot \sqrt{\pi} \cdot V_{\text{ring}}} \cdot \exp\left[-\frac{t^2}{(\tau_{\text{pump}}/2)^2}\right]\end{aligned}\quad (2.6)$$

where  $\Delta N$  is the change in free-carrier concentration,  $\tau_{\text{extract}} = 50$  ps is the extraction time with a reverse-bias of 10 V,  $\tau_{\text{open}} = 1190$  ps is the open-circuit extraction time,  $n$  is the number of photo-excited carriers per unit volume,  $\tau_{\text{probe}} = 32.3$  ps is the resonant cavity lifetime,  $N_{\text{ph}}$  is the total number of absorbed photons,  $V_{\text{ring}}$  is the volume of the ring resonator, and  $\tau_{\text{pump}} = 10$  ps is the pump pulse duration. From Eq. (2.6), the change in the refractive index and optical absorption of the silicon ring waveguide is obtained [25]. These changes are applied to an analytical model of the ring resonator transmission response to obtain the theoretical temporal response of the probe signal [30]. From this model we determine that the probe resonance is shifted by  $\Delta\lambda = -0.044$  nm, which corresponds to an effective index change of  $\Delta n_{\text{eff}} = -1.12 \cdot 10^{-4}$ , or equivalently to a refractive index change in the silicon waveguide of  $\Delta n_{\text{Si}} = -1.08 \cdot 10^{-4}$ . This refractive index change is caused by a maximum carrier concentration of  $\Delta N = \Delta P = 1.93 \cdot 10^{16} \text{ cm}^{-3}$  [25]. We estimate that the amount of pump pulse energy absorbed inside the ring to excite such a carrier concentration is only 41 fJ. Thus, only a small portion of the pump power is actually absorbed. The remaining pump power, which is necessary for the two-photon absorption effect [16], is scattered off the ring in this device. By adding another adjacent waveguide to the ring this scattered pump power could be recycled for use with other modulators on the same chip. The amount

of probe absorption induced by the excited free-carrier concentration is estimated to be only  $\Delta\alpha = 0.3 \text{ cm}^{-1}$  [25], which has the effect of reducing the achievable modulation depth by only 3.4%.

For a given modulation depth the required pump energy increases as a function of the applied reverse-bias. This is because the faster the carriers are extracted the smaller the maximum carrier concentration is (and, in turn, refractive index change). Thus, more pump energy is needed to achieve the same modulation depth. Using the carrier extraction times shown in Figure 2.12 and the theoretical model described above, the absorbed pulse energies required to maintain the same amount of modulation depth (MD = 84%) are obtained for different applied reverse-bias voltages. Note that here we show only the energy absorbed by the pump pulse, not the total pump energy. In the inset of Figure 2.13 we show the required pump energy as a function of the applied voltage. Errors bars are derived from uncertainty in the extraction times in Figure 2.12. It is seen that the required pump energy increases linearly with voltage; a modulator operating under a 15 V reverse-bias voltage requires almost twice the amount of energy than a modulator under 0 V bias. Also shown are the experimentally derived absorbed pulse energies for four different reverse-bias voltages (triangles), as obtained from the measured diode currents, showing good agreement with the calculations.

The device we have demonstrated can be used as a modulator in all-optical networks. The modulation bit-rate of the device is determined by the carrier extraction time. Using a micron size ring resonator, under a reverse-bias voltage of 10 V, a bit-rate of 5 Gbit/s is possible [44]. Such a rate would be realizable if the diode were to encompass the entire ring. We estimated that the pump energy needed to be coupled into the ring resonator at this bit-rate is as low as 2.2 pJ [20]. This estimated energy is

lower than the one used in this work (19 pJ) because the pump pulse used here has a bandwidth of 0.37 nm, which is approximately 4.4 times wider than the devices pump resonance. Thus, less than a quarter of the pump energy was actually coupled to the ring. A pump beam with a sufficiently narrow bandwidth, operating at a 5 Gbit/s bit-rate, would require an average power of only 11 mW, which is easily achievable using fiber based amplifiers.

## 2.4 SUMMARY

In this chapter we demonstrated all optical switching using a photonic crystal nanocavity. The devices size is on the order of the diffraction limit of the light confined within it. By minimizing the devices size low switching powers can be achieved. Here the required switching energy was comparable to previous larger devices because the quality factor of the device was quite low. However, in the future a photonic crystal nanocavity with a Q-factor on the order of a million, as has recently been demonstrated [13], could be used in order to demonstrate sub-femto-Joule switching.

We also demonstrated ultra-fast all-optical switching of a ring resonator device by integrating a PIN-diode around the ring waveguide. By reverse-biasing the diode we were able to sweep the injected carriers out in times shorter than 25-picoseconds, enabling 20+GHz all-optical switching/modulation on a silicon chip.

## CHAPTER 3

### EVOLUTIONARY ALGORITHMS FOR NANOPHOTONICS

#### 3.1 INTRODUCTION

It isn't always straightforward as to how to design a nanophotonic device to have the best possible performance. In the past nanophotonic device designers have started with something that works reasonably well and then iteratively tweaked the design by trial and error. However, this trial/error process is time consuming, random and the new design typically isn't the best possible one. Even though it is possible to automate this simple search process and with a few tricks improve it slightly, in the end it just isn't efficient.

Recently there has been significant interest in a class of global search algorithms known as evolutionary/genetic algorithms. The beauty of evolutionary algorithms is that they are simple to implement, they don't require extensive problem specialization and they are generally quite good at finding the "globally best" solution (it is usually impossible to truly know if the solution is really the globally best). Evolutionary algorithms are inspired by natural evolution and operate by repeatedly selecting, varying, and replicating successful individuals in a population of candidate solutions [45-47], or otherwise simply put - the survival of the fittest. These algorithms are well suited for finding solutions to problems that involve very large and complex search spaces that do not have smooth gradients leading to an optimum. In particular, evolutionary algorithms are well suited for searching open-ended design spaces that are not conveniently characterized by a finite set of parameters, but are spanned instead by an unbounded set of features or primitives, such as the design space of arbitrary functional geometries and morphologies [48].

Evolutionary Algorithms have been shown to be an effective method for solving problems in nanophotonics. They have been applied to design waveguide and photonic crystal based spot-size converters [49, 50], fiber Bragg gratings [51], transitions between traditional index-guided and PC waveguides [52] and photonic crystal band gaps [53]. However, these previous works have used evolutionary algorithm implementations where the devices are represented using a simple binary bitmap. In this chapter, using a test problem, I will show that this is usually not the best design representation and I will present an alternative representation based on trees that is inspired by genetic programming [46]. This new tree representation enables the discovery of devices that outperform human designs.

The test problem I will investigate in this chapter is the maximization of the band gap of a two-dimensional photonic crystal [54]. I would like to note that after this initial demonstration our group has successfully used evolutionary algorithms to demonstrate ultra-small mode volume nanocavities by exploiting the electric field discontinuity at dielectric interfaces [55], to demonstrate efficient grating couplers, and to demonstrate light localization in pseudo-random dielectric configurations [56].

### 3.2 MAXIMIZING PHOTONIC CRYSTAL BANDGAP

Photonic crystals are structures that possess a photonic bandgap – a range of frequencies where light is forbidden from propagating in the crystal [57-59]. By creating defects in the photonic crystal, light with a frequency in the bandgap can be guided or trapped, enabling the control of the flow of light on the nanoscale. It is interesting to note that the first photonic crystals were not designed and fabricated in a laboratory but were evolved over millions of years in nature. They create the beautiful colors in butterfly wings [60, 61] and are even found in creatures of the sea such as the

Sea Mouse [62]. Photonic crystals have traditionally been hand-designed by trial and error with some insight from the extensive research of crystalline atomic lattice structures [58, 63]. This has yielded simple lattices and unit cells, such as a square lattice of cylinders [59]. The large bandgap of these photonic crystals has been achieved by varying the parameters of the lattice [64], however, it is not known whether these simple structures truly achieve the maximum bandgap for a given index contrast.

In this chapter we use an evolutionary algorithm (EA) to systematically search for photonic crystals with maximal bandgaps [47]. Evolutionary algorithms have been shown to be effective tools for exploring hard design challenges, and have recently proven to be an effective design automation tool that can sometimes outperform human designs [46, 54]. The evolutionary algorithm used here starts with a population of randomly generated photonic crystals that in general possess no bandgap. The fittest photonic crystals, those approaching higher band gaps, are selected and mated with each other. During mating the elements of the parent photonic crystals are crossed over (swapped), and are then subject to mutation (randomly changing high/low dielectric constants). This process is repeated for many generations after which we find photonic crystals that not only have bandgaps, but also have bandgaps larger than the ones created by humans.

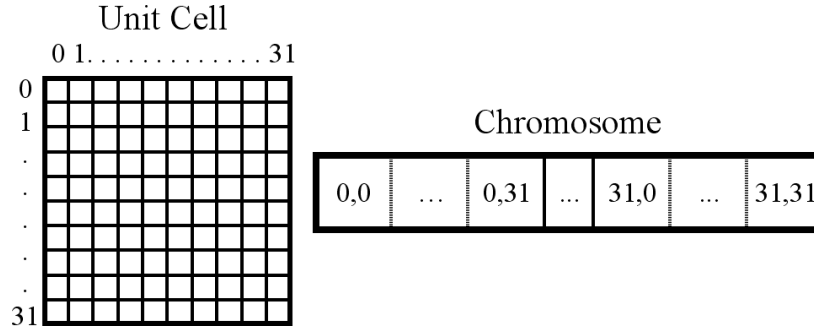
We should note that similar works have been attempted before. However, they seeded the evolutionary algorithm with a human made photonic crystal with a known bandgap, in turn, the evolutionary algorithm only optimized the bandgap of the seed crystal [53]. In this work, we are able to achieve large bandgaps without seeding, opening the possibility for the algorithm to discover photonic crystals that would have never otherwise been imagined by humans. In addition, the previous work focused on

higher energy bands [53]. In contrast, here we focus on a bandgap between the first two bands because the lower energy bandgap will fall under the light-line, enabling practical fabrication of the designed photonic crystal in a thin dielectric slab system [58].

### 3.3 METHODOLOGY

In this chapter the unit cell is the element of the photonic crystal that is subject to evolution. The unit cell is discretized by a 32x32 grid of square pixels that can each either have high (3.4 - Silicon) or low (1 - Air) dielectric material. To apply the evolutionary algorithm to the design of the photonic crystal, the unit cell is represented by a chromosome – a blueprint of the makeup of the cell. We look at two types of chromosome representations in this chapter: bitmaps (direct encodings) and trees (generative encoding). Both bottom-up and top-down trees are explored.

The bitmap representation consists of a binary string of length 1024 (32x32) where a ‘1’ corresponds to high dielectric material, and a ‘0’ corresponds to a low dielectric material. Each bit in the binary string corresponds to a unique grid point of the 32x32 unit cell, as shown in Figure 3.1. In this representation there are  $2^{1024}$  possible photonic crystals. Such a large number of possible photonic crystals are impossible to explicitly search, in turn, pointing out the necessity for an evolutionary algorithm to discover the best photonic crystal design.

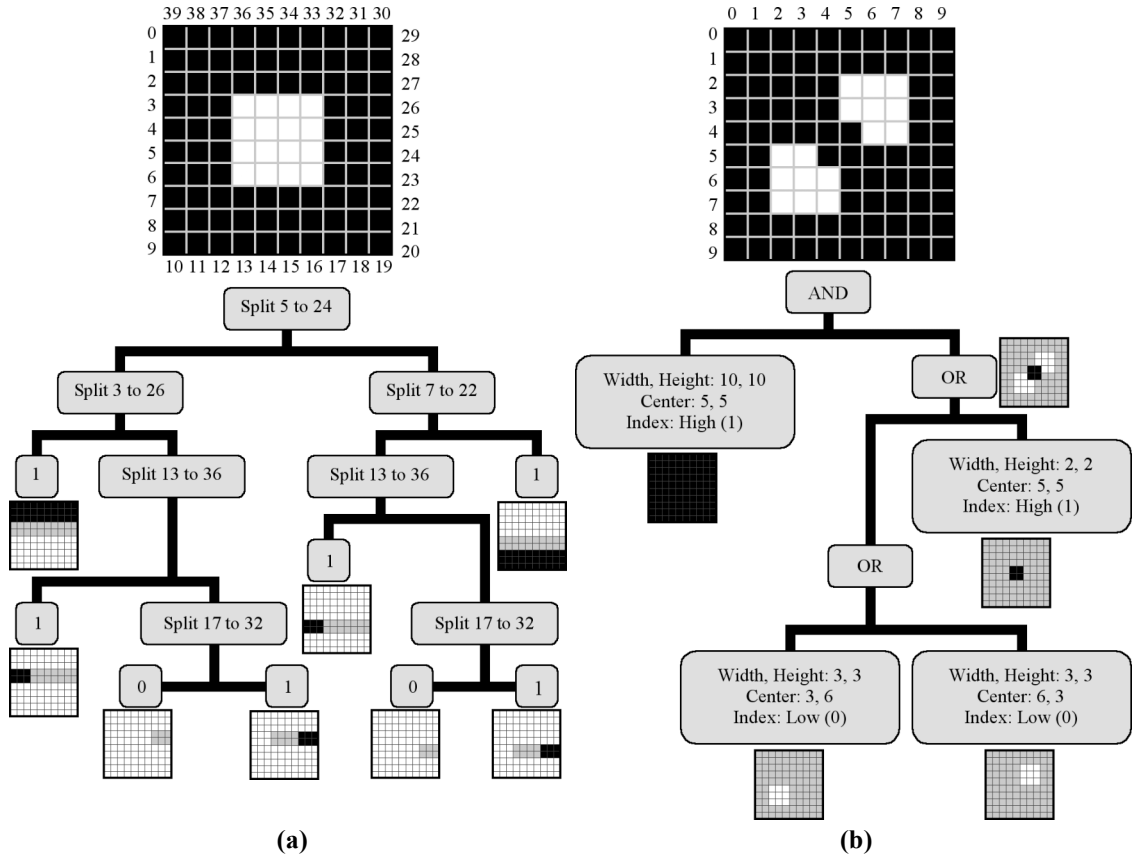


**Figure 3.1.** A unit cell discretized onto a 32x32 grid and its associated binary string. The binary string encodes the unit cell row –by- row. Each pixel in the unit cell is assigned to be high (1) or low (0) dielectric material (from [54]).

The tree representations define the unit cell using ‘clumps’ of high or low dielectric material. This is a much more efficient representation, since photonic crystals generally have clumps of dielectric material, as opposed to isolated pixels. This efficiency allows the evolutionary process to better exploit the substructure of the search space. In the top down tree representation the unit cell is recursively split into subdivisions by partition lines, starting at the top of the tree and going down. At the bottom of the tree are terminal nodes that determine the dielectric material (0 or 1) of the corresponding subdivision. The lines that split the unit cell are uniquely identified by their start and end points, where the start and end points lay on the outside perimeter of the unit cell. Tree nodes to the right of a split are inclusive, so that all pixels that have a position ‘greater than or equal’ to the split-line are included. Tree nodes to the left of a split are exclusive, so that all pixels that have a position ‘less than’ the split-line are included. An illustration of this representation and how it is interpreted into the pixilated unit cell is shown in Figure 3.2a.

In the bottom-up tree representation rectangles of dielectric material are recursively combined to form a larger structure. The rectangles are defined by a width





**Figure 3.2.** (a) Illustration of an example 10x10 unit cell (32x32 is used with the evolutionary algorithm) and a top-down tree that can be used to construct this unit cell. The black (white) pixels are high (low) index material. The numbers label the perimeter of the unit cell. Starting at the top of the tree and going down, each split, a dividing line uniquely defined by two perimeter pixels, sections the unit cell into ever-smaller areas. The terminal nodes assign dielectric material (i.e. high or low) to these areas. Next to each terminal node is an illustration of the result. Light-gray coloring designates the sub-area that has been defined by the splits (i.e. the terminal nodes sibling ‘acts’ on this light-gray area). The complete unit cell is obtained by combining all of the sub-areas into one. (b) Illustration of an example 10x10 unit cell (32x32 is used with the evolutionary algorithm) and a bottom-up tree that can be

used to construct this unit cell. The numbers around the unit-cell label the x-y grid. Starting at the bottom of the tree and going up, rectangles defined by a width, height, center and index are combined using boolean AND and OR operator nodes. The illustrations next to the nodes show how the rectangles are defined and combined to obtain the unit cell. The light-gray coloring indicates that those pixels are undefined and the boolean operators subsequently have no effect on them (i.e. defaults to OR). If there are any undefined pixels in the resulting unit cell, they are automatically set to be low index material (from [54]).

and height, center, and a dielectric material (0 or 1). Going up the tree, the rectangles are combined by the Boolean operators AND and OR. An illustration of this representation and how it is interpreted into the pixilated unit cell is shown in Figure 3.2b.

The evolutionary algorithm used here operates in the following steps:

**Step 1: Initialization.** The evolutionary algorithm starts with a population of 100 randomly generated chromosomes. In the bitmap representation each pixel in the unit cell has a 50% probability of being high or low index material. In the top down tree representation, the top node is a randomly generated split. The children nodes are randomly generated to be a split, or a high or low index terminal node, all with equal probability. In the bottom up representation, the top node is a randomly generated boolean operator. The children nodes are randomly generated to be one of the boolean operators, or a rectangle of dielectric material, with equal probabilities.

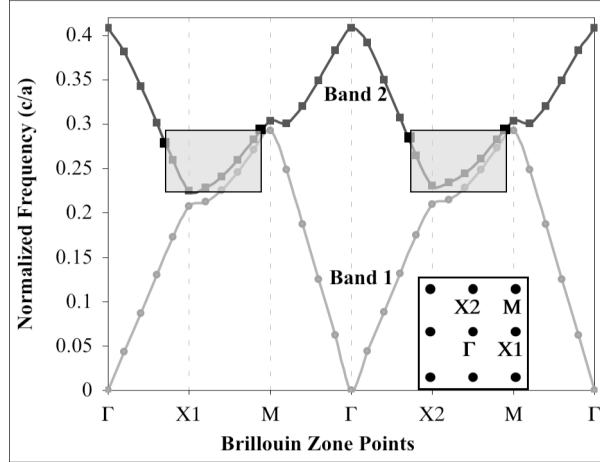
**Step 2: Fitness evaluation.** Each chromosome in the population is then converted into a 32x32 unit cell. The high (low) index pixels are assigned an index of 3.4 (1). The

unit cell is then repeated on a square lattice of period  $a$ . Next, the bands of the photonic crystal are calculated and any bandgap (or lack of) is obtained. A software package was used to solve for the bands of the photonic crystal by preconditioned conjugate-gradient minimization of the block Rayleigh quotient in a planewave basis [65].

In previous works the fitness criteria used was the gap to mid-gap ratio [53]:

$$\text{Fitness} = \frac{E_{top} - E_{bottom}}{E_{middle}} \quad (3.1)$$

where  $E_{top}$ ,  $E_{bottom}$ ,  $E_{middle}$  are the top, bottom and the middle of bandgap, respectively. However, since the initial population of randomly generated photonic crystals in general *does not* possess a bandgap, they were artificially assigned a small fitness value [53]. A search using such a fitness criterion has no gradient to follow during the initial phase, and therefore drifts blindly in the search space. The lack of gradient may explain why the previous attempt that used this fitness criterion eventually needed to seed the population with a hand-designed solution with an existing bandgap. In this work we have developed a fitness criterion that is suitable for crystals that do not already possess a bandgap, thereby enabling the discovery of new types of photonic crystal structures from scratch. Our measure of fitness is the amount of overlap of the top and bottom bands, here referred to as the overlap area. Since no assumptions were made about the symmetry of the unit cell it is necessary to calculate the bands over the entire first brillouin zone. Figure 3.3 shows a band diagram for a randomly generated photonic crystal that does not possess a bandgap. Only the first brillouin zone points along the  $\Gamma \rightarrow X1 \rightarrow M \rightarrow X2 \rightarrow \Gamma$  quadrant are shown for compactness. It is clear that there is no bandgap between the bands but there is a significant overlap. The amount of overlap is defined by an overlap area:



**Figure 3.3.** Band diagram of a randomly generated photonic crystal with no bandgap. The vertical axis is the frequencies normalized to  $(c/a)$  where ‘ $c$ ’ is the speed of light and ‘ $a$ ’ is the lattice period. The horizontal axis are the brillouin zone points. The inset shows the reciprocal lattice and the corresponding Brillouin zone points. The shaded light-gray boxes indicate the areas where the two bands overlap each other. The bounds of the boxes are obtained from the points in the band diagram where the top band is below the top of band 1. The height of the boxes is always the same; it’s defined from the bottom of band 2 (here at the X1 point) to the top of band 1 (here at the M point). The width is from the left-most to the right-most points (including the interpolated ‘half-way’ points) that fall below the top of band 1. The total overlap area (Eq. (3.2)) can be obtained from the sum of the areas of the individual shaded boxes (from [54]).

$$\text{Overlap Area} = \frac{E_{top,1} - E_{bottom,2}}{(E_{top,1} + E_{bottom,2})/2} \cdot \frac{N_{overlap}}{N_{total}} \quad (3.2)$$

where  $E_{top,1}$  is the top of the bottom band,  $E_{bottom,2}$  is the bottom of the top band,  $N_{overlap}$  is the number points in the band diagram where the top band is below the top of the bottom band, and  $N_{total}$  is the total number of points (i.e. the individual dots in Figure 3). To improve the speed of the band calculations, only four points between

each Brillouin zone symmetry point (i.e.  $\Gamma$ , X1, M, X2) was calculated, so an additional point is linearly interpolated ‘half-way’ between each one of the points. This interpolation is shown in Figure 3.3 where the left and right edges of the two overlap areas don’t fall on points that were actually calculated, they fall on the ‘half-way’ points, as indicated by the bold square points (these are the only half-way points shown on this diagram). For photonic crystals that do possess a bandgap, the traditional fitness criteria (Eq. (3.1)) is used.

**Step 3: Selection.** The 100 chromosomes are then selected for the next generation using a fitness-dependent selection criterion. Two selection methods were used: The first is rank selection, where the likelihood of an individual being selected is proportionate to its rank in the population (i.e. the photonic crystals are ranked from largest to smallest overlap to smallest to largest bandgap). A stochastic-uniform-sampling (SUS) method was used to implement the selection in a way that guarantees minimal selection noise [47]. The second selection method used was deterministic crowding (DC) [66], which helps maintain diversity of solutions by comparing solutions only to those that are most similar to them. Diversity of solutions in the population must be maintained if crossover-operators are expected to produce anything new. Selected chromosomes become the parents for a new generation of chromosomes.

It is important to ensure that the fitness of the population does not decrease in the newly created population. This is done by practicing elitism – a random chromosome in the new population is replaced with the best chromosome from the previous generation.

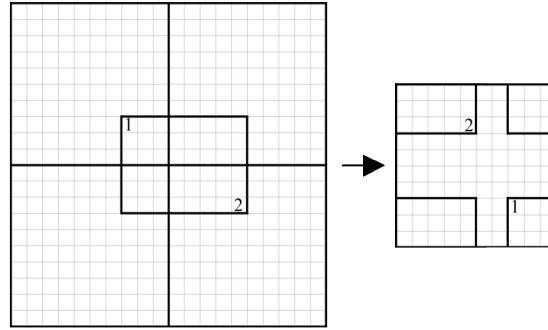
**Step 4: Variation.** Two new offspring are created from two selected parents. To create the child chromosomes, portions of the two parent chromosomes are crossed over with a crossover probability of 70% (i.e. 30% of the time the children are exact copies of the parents). In the bitmap representation, two random points in the 32x32 unit cell are picked. All of the pixels in the rectangle defined by these two points are swapped between the parents to create the new children. The order of the two points (i.e. point 1 or 2) determines how the rectangle is defined. If point 2 is farther away from the origin (i.e. greater) than point 1, then the rectangle spans from point 1 (upper-left corner of rectangle) to point 2 (lower-right corner of rectangle). If point 2 is closer to the origin than point 1, then the rectangle spans from point 1 in one unit-cell to the neighboring unit-cells. However, since the chromosome only encodes the one unit-cell and not a periodic array of them, the rectangle must be wrapped back into the one unit-cell (i.e. where point 1 is). This is done by moving the portions of the rectangle in the neighboring-cells to their equivalent positions in the ‘main’ unit-cell, as illustrated in Figure 3.4 In the tree representations, a random node in each of the two parent trees is selected. Then the nodes and all of their respective children are swapped between the two parents trees to obtain the two new children.

In the next step of variation the chromosomes in the new population are mutated. In the bitmap representation, each bit in the 1024 bit long chromosome is subject to be flipped from a 0 to a 1 or vice versa with a mutation probability of 1%. In the tree representations, each node in the tree is mutated with a probability of 1%. The manifestation of the mutation depends on the type of node. For a split node, the start and end points are randomly offset by  $\pm 1$  or 0, each with an equal probability. A terminal node can switch from high to low dielectric material or vice-versa. A Boolean operator node can switch from AND to OR or vice-versa. And lastly, for a rectangle

node, the width, height, and center can each be offset by  $\pm 1$  or 0, with equal probability.

In tree representations variation is followed by pruning in order to keep the tree from becoming overly large. Unfortunately the pruning has the unwanted effect that it may blindly destroy a tree that would otherwise have a very high fitness. To minimize this risk the number of levels that the trees are pruned to was tuned over many trials to minimize the effect. Elitism also helps to minimize the risk.

**Step 5:** Repeat from step 2 until a stopping criterion is met.

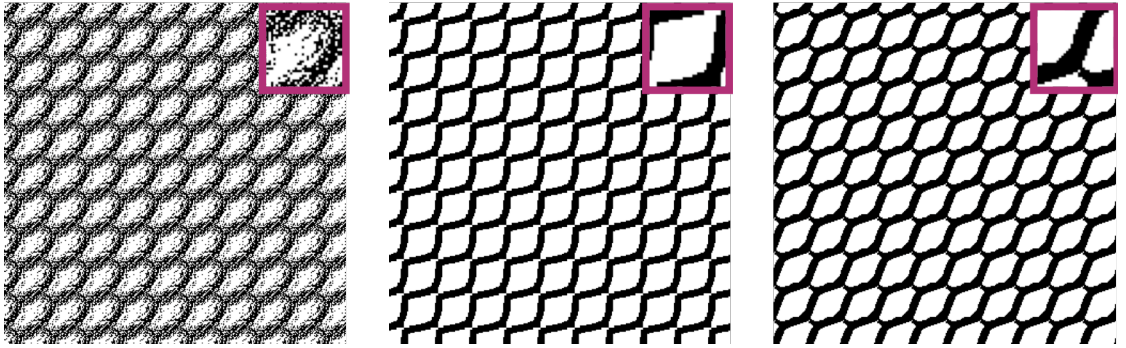


**Figure 3.4.** An example rectangle that spans from point 1 in the ‘main’ unit-cell to points in the neighboring unit-cells. This representation is equivalent to a rectangle that spans the corners of the ‘main’ unit-cell (from [54]).

### 3.4 RESULTS AND DISCUSSION

The evolutionary algorithm was run for 1500 generations to obtain large bandgaps for the TE Polarization (electric field in the plane of the photonic crystal) of light. The evolutionary algorithm could easily be applied to the TM polarization, as

well. First we consider the evolutionary algorithm using the stochastic-uniform-sampling selection criterion (SUS). After the 1500 generations, using the bottom-up tree and top-down tree representations, the SUS evolutionary algorithm yielded photonic crystals with bandgaps as large as 30.86% and 31.89%, respectively, as shown in Figure 3.5. The band diagram for the top-down tree photonic crystal is shown in Figure 3.6. However, the bitmap representation achieved a bandgap of only 5.12%. This was improved upon by using a coarser grid of 16x16 pixels, as shown in Figure 3.7.

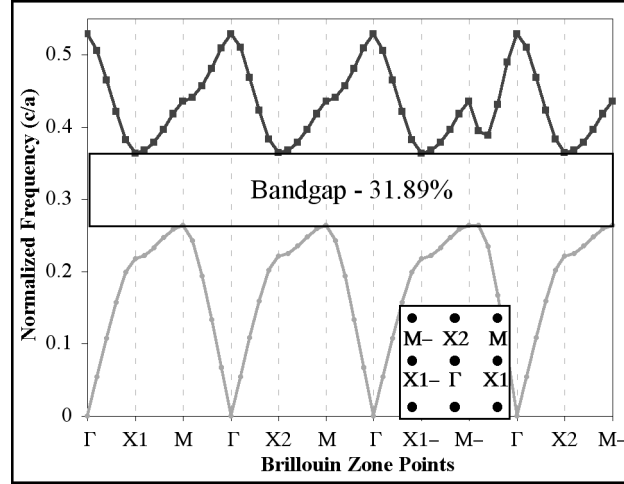


**Figure 3.5.** Photonic crystals and unit-cells (insets) created by the SUS evolutionary algorithm. From left to right: Bitmap Representation (5.12% Bandgap), Bottom up tree (30.86% Bandgap), Top down tree (31.89% Bandgap) (from [54]).

It is clear from these results that the tree representations considerably outperformed the bitmap representation. This is because the trees are able to encode the information in the unit-cell much more efficiently than a bitmap. The bitmap representation yields a lot of extra ‘noise’, or random pixels that degrade the quality of the photonic crystal, as seen in Figure 3.7 and especially in Figure 3.5 where the search space is extremely large ( $2^{1024}$  possible solutions). The random pixels effectively reduce the index-contrast, so by manually removing the noise the bandgap



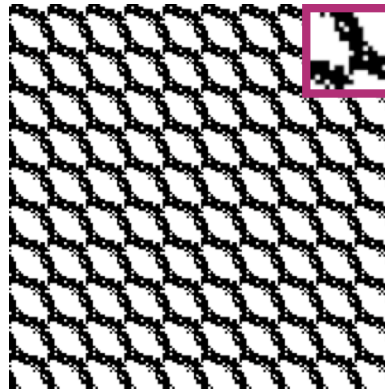
can be improved considerably (even for the 32x32 grid where there clearly is a photonic crystal that is capable of supporting a bandgap, there is just too much noise), but doing so is time-consuming and undesirable for general design purposes. The tree representations are much less susceptible to this noise problem since they deal hierarchically with ‘clumps’ of dielectric material as opposed to individual pixels.



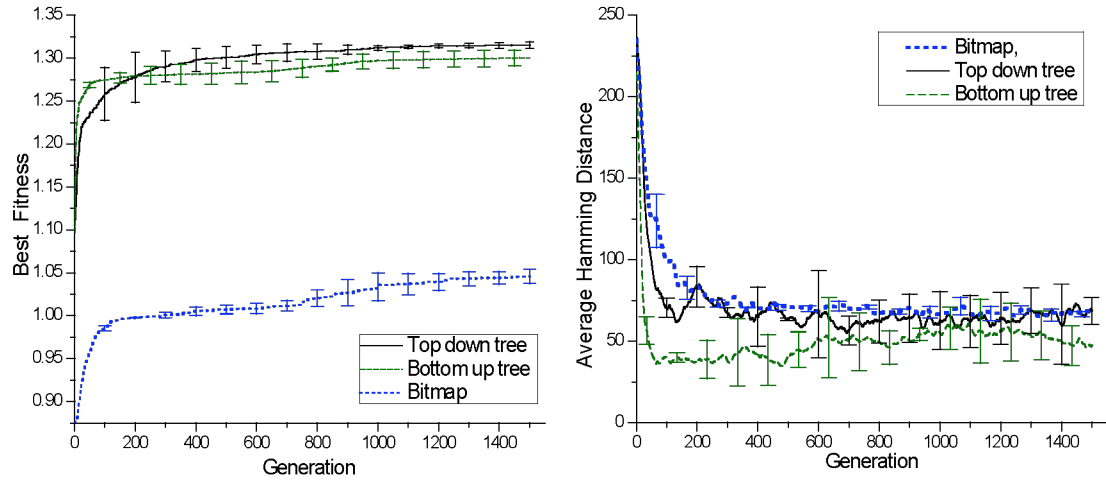
**Figure 3.6.** Band diagram of the photonic crystal discovered by the SUS evolutionary algorithm using a top down tree representation. The vertical axis is the frequencies normalized to  $(c/a)$  where ‘c’ is the speed of light and ‘a’ is the lattice period. The horizontal axis is the brillouin zone points. The inset shows the reciprocal lattice and the corresponding Brillouin zone points (from [54]).

Figure 3.8 shows some performance metrics of the SUS evolutionary algorithm, plotted as function of generation. Figure 3.8a shows the best fitness for the different representation types. For fitness values below 1 the fitness is the overlap area, for values above 1 the fitness is the bandgap, i.e. a fitness of 1.25 is a bandgap of 25%. Figure 3.8b shows the average hamming distance of the population. The hamming distance is a measure of how different the photonic crystals in the population

are. The larger the hamming distance, the more diverse the population. It is important to maintain a diverse population as long as possible because otherwise the growth of the over-all population is stunted since all of the photonic crystals become essentially the same. Once the crystals are very similar, crossover between parents becomes rather ineffective. Consequently, the algorithm may prematurely converge to only a local maximum, rather than a global maximum. It is clear from Figure 8 that the evolutionary algorithm converges to a solution rather quickly, within only 100 generations. This is a weakness of the stochastic-uniform-sampling evolutionary algorithm. We now consider another type of selection criterion, deterministic crowding, that is slower to converge but is able to maintain a very diverse population, thereby delaying convergence and promoting useful crossover.



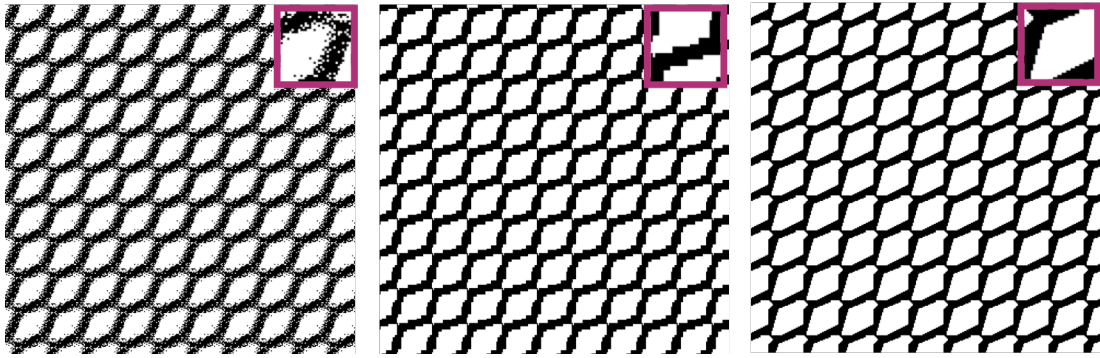
**Figure 3.7.** Photonic crystal and the unit-cell (indent) obtained using the bitmap representation with a 16x16 grid. The bandgap of the photonic crystal is 21.92% (from [54]).



**Figure 3.8.** Search performance of the SUS evolutionary algorithm. (a) Best fitness as a function of generation for each of the chromosome representations, (b) Average hamming distance as a function of generation. The curves were smoothed for presentation purposes. Error bars are derived from three independent runs started from randomized initial populations.

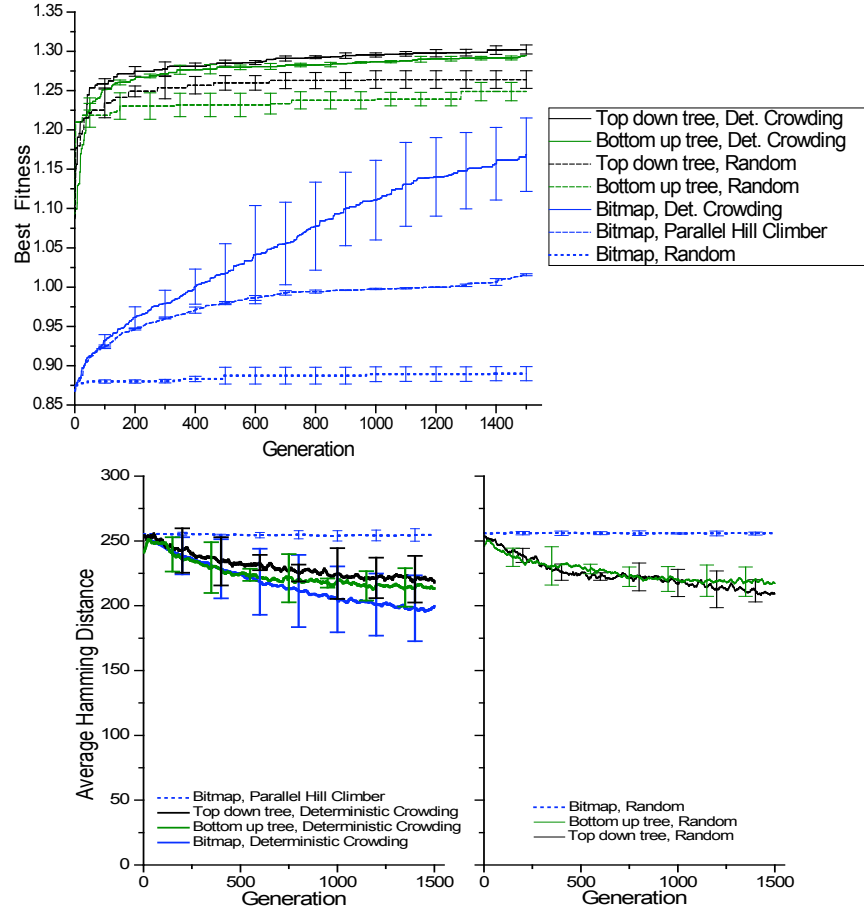
Figure 3.9 shows the results of the deterministic crowding evolutionary algorithm for the different types of chromosome representations. Using the bottom-up tree and top-down tree representations, the evolutionary algorithm yielded photonic crystals with bandgaps as large as 29.7% and 30.73%, respectively, comparable to the bandgaps achieved using stochastic-uniform-sampling. However, now the bitmap representation is able to achieve a bandgap as large as 21.32% on a 32x32 grid. The performance metrics are shown in Figure 3.10. The results are also compared with a completely random search (i.e. step 1 and 2 are repeated). The bitmap approach was also compared with a parallel hill climbing algorithm (i.e. the unit cells are randomly mutated, if there was an improvement the photonic crystal is kept, otherwise discarded). As seen in Figure 3.10a, the deterministic crowding evolutionary algorithm outperforms a completely random search for all of the representation types,

consequently stochastic-uniform-sampling does too (See Figure 3.8). The evolutionary algorithms using the bitmap representation also outperform the parallel hill climbing algorithm, which only reaches a maximum bandgap of 1.71%. Figure 3.10b confirms that the deterministic crowding evolutionary algorithm is able to maintain a high-degree of diversity throughout all of the generations, enabling the vast improvement in the bitmap representations performance. However, when using the tree representations, deterministic crowding didn't offer a performance advantage over stochastic-uniform-sampling, even after 1500 generations.



**Figure 3.9.** Photonic crystals and unit-cells (insets) created by the deterministic crowding evolutionary algorithm. From left to right: Bitmap Representation (21.32% Bandgap), Bottom up tree (29.7% Bandgap), Top down tree (30.73% Bandgap) (from [54]).

As seen in Figure 3.10a, the random search (i.e. step 1 and 2 are repeated) achieved a best bandgap of 27.16% when using the top down tree representation. This is much better performance than all of the results obtained when using the bitmap representation. The reason for this is because of the tree representations efficient encoding of the unit cell. Despite the size of the grid, trees enable for an open-ended

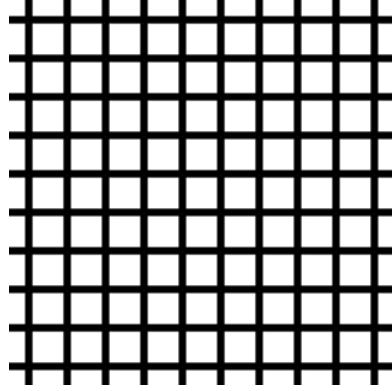


**Figure 3.10.** Performance metrics for the deterministic crowding algorithm with the different chromosome representations. Comparisons to a random search algorithm and parallel hill climbing algorithm (only for the bitmap approach) are shown. a) Best fitness as a function of generation. The ordering in the legend corresponds with the ordering of the fitness's on the graph (from best to worst). b) Average hamming distance as a function of generation. The curves were smoothed for presentation purposes. The left graph includes deterministic crowding and parallel hill climber. The right includes only random searches. Error bars are derived from three independent runs started from randomized initial populations.

design space – i.e. the number of grid points can quadruple yet the tree is still able to encode the entire unit-cell without changing. The bitmap representation is plagued by ‘rogue’ pixels that reduce the effective index of the unit-cell, and this problem gets worse the finer the grid gets. Thus, the bitmap representation is best used with very coarse grids. Despite the very good performance of the random tree search, it is clear that an evolutionary algorithm was still needed to discover photonic crystals with even larger bandgaps.

We observed that the cross-over from a fitness below 1 to above 1 is very predictable (i.e. the population has no bandgaps and then develops bandgaps). A photonic crystal that may have a fitness of 0.98 in a previous generation (i.e. little to no overlap of the bands), after being crossed over and mutated with another parent *will* develop a small bandgap ( $\sim 1\%$ ) in the next generation (of course, it’s possible that after crossover and mutation that its fitness will decrease but *eventually* the right mating will occur), and consequently after many such generations develop into a photonic crystal with a rather large bandgap. This progression is predictable because as the photonic crystal bands develop less and less band overlap, structures evolve in the unit-cell that are able to support a bandgap. The bandgap arises once the structure is fine-tuned and the overall index-contrast is increased and subsequently the noise level is reduced. Even though the bitmap representation yielded a small bandgap when using a 32x32 grid and stochastic-uniform-sampling, the structure of a photonic crystal that *could* yield a large bandgap is very clearly seen in the noise of Figure 3.5. The evolutionary algorithm in fact found the correct structure; it was just unable to properly deal with the large amount of noise. This predictability shows that our overlap area fitness criteria is excellent for obtaining photonic crystals with large bandgaps when starting from ‘random noise’, and consequently without seeding.

The best published human design for a photonic crystal using a square lattice and the TE polarization is shown in Figure 3.11. It has a bandgap of 28.35% for this index contrast (3.4 to 1) [64]. Our evolutionary algorithm has found photonic crystals that improve over this design by 12.5%. The evolutionary algorithm achieved this by not optimizing the human-designed structure but by finding new types of photonic crystal structures altogether. As seen in Figure 3.5 and Figure 3.9, the discovered photonic crystals are highly-skewed and non-uniformly scaled. It has previously been shown that the bandgap of simple photonic crystals can sometimes be improved by reducing the symmetry of the unit cell and the lattice [64, 67, 68]. By making no assumptions about the symmetry of the unit cell, our evolutionary algorithm has found that the photonic crystals with the largest bandgaps tend to share this characteristic. This result has also been observed in nature, the photonic crystals in butterfly wings also exhibit a lack of strong symmetry and non-uniform scaling [60, 61]. Lastly, the largest known photonic crystal bandgap for TE polarization is obtained using a triangular lattice (a square lattice was used here) of hexagonal air holes embedded in a high index background, which resembles a honeycomb structure [64]. Here, with the constraint of a square lattice, the EA attempted to recreate this structure as seen in Figure 3.5. However, the resulting honeycombs are not symmetric; they are skewed and non-uniformly scaled. By doing so the EA was able to find structures that improve over the best human design for a square lattice.



**Figure 3.11.** Best human designed photonic crystal with a bandgap of 28.35%. The photonic crystal is a square lattice of square air (index -1) holes of width and height  $0.8*a$  ( $a$  is the periodicity of the lattice) embedded in a background of high index material (index - 3.4).

### 3.5 SUMMARY

We have demonstrated the ability to use evolutionary algorithms to discover novel photonic crystal structures with large bandgaps. Starting with a completely random population of photonic crystals that possess very small or even no bandgaps, we obtain photonic crystals with larger bandgaps than the best human design. We compared two types of selection criteria, stochastic-uniform-sampling and deterministic crowding, and two chromosome representations, bitmaps and trees. Each selection method and representation has advantages and disadvantages; so, future problems must be evaluated to determine the best approach for the problem. In practice, a combination of these techniques may yield the best results. For example, a bitmap representation would work very well for fine-tuning small regions of the unit-cells obtained from the tree representations. In conclusion, we've shown that evolutionary algorithms can be used as a robust design and optimization tool in the field of photonics.



## CHAPTER 4

### ADIABATIC WAVELENGTH CONVERSION

#### 4.1 INTRODUCTION

I wanted to answer a simple question – if there is light trapped in a resonator and then the resonator is tuned to a new resonant frequency, what happens to the light? Does it simply dissipate away because the light and the resonator are no longer in sync? The answer to this question surprised me – it turns out that the light actually *changes* its frequency in order to follow the state of the resonator. The remainder of this chapter is devoted to how this occurs and the experimental demonstration of this wavelength conversion technique.

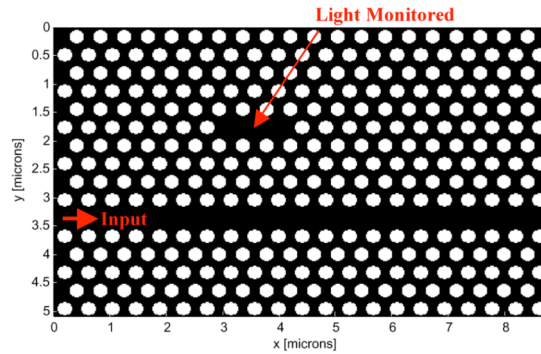
Previous approaches to wavelength conversion on a silicon chip rely on non-linear effects such as cross-gain modulation, cross-phase modulation, cross-absorption modulation, four-wave mixing, difference frequency generation [69-72], or free carrier effects [73]. However, all of these approaches have one thing in common – they are fundamentally all-optical, i.e. they operate by imparting the optical signal carried by a high intensity pump beam onto a probe beam. In contrast, in this chapter we present a new way to change the frequency of light based on the dynamic tuning of a resonant cavity where the wavelength of the light can be tuned using *any* means, including electrically, optically or even mechanically.

It is well known that tuning the parameters of an optical cavity induces *filtering* of different colors of incident light [74]. Here we demonstrate that tuning the parameters of the cavity also *changes* the frequency of any trapped light. This is an effect often observed with classical oscillators, such as a guitar string. For example if we pluck the guitar string we generate a sound wave at a particular frequency. Now, before the strings vibration dies out, we change length of the string by moving our

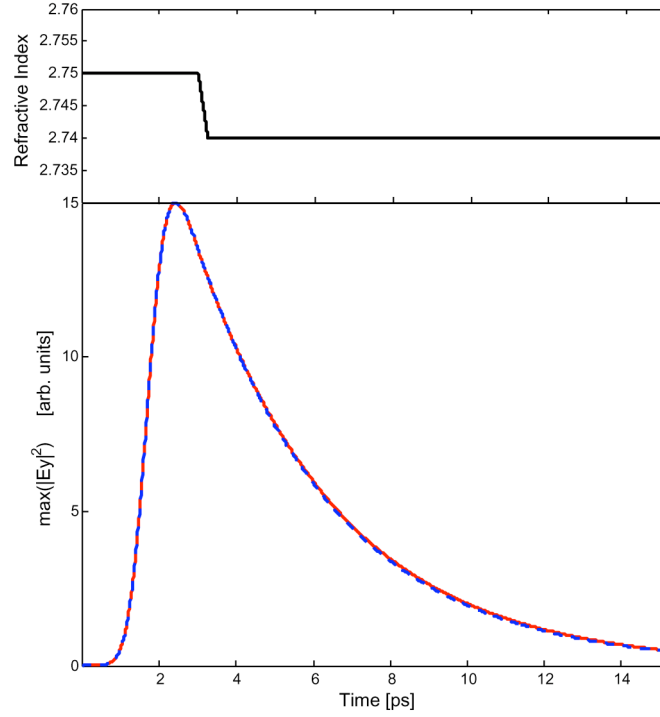
finger or turning the tuning peg. As the length of the string is changed the frequency of the sound wave changes. Or in other words the sound's frequency follows the state of the resonant guitar string. Here we are doing the same thing but instead are dynamically tuning a micro-optical resonator in order to change the frequency of light.

## 4.2 THEORY AND SIMULATIONS

In order to investigate this effect, consider the photonic crystal resonator shown in Figure 4.1. The structure consists of a line defect waveguide and a point defect cavity created by ‘removing’ three air holes. The photonic crystal has a lattice constant of  $a=420$  nm and the air holes have a radius of  $r=130$  nm. We used 2D FDTD simulations for our analysis. The refractive index of the background is set to  $n=2.75$ , which is a good effective index approximation of an air-bridge slab with an index of 3.5. We found that the resonator has a resonance at  $\lambda_{\text{res}}=1525$  nm with a quality factor of  $Q=4000$ .



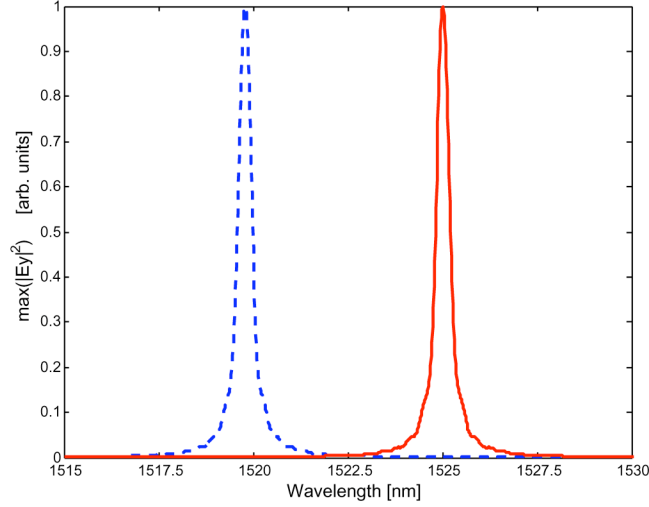
**Figure 4.1.** Photonic crystal resonator used for wavelength conversion (Black –  $n=2.75$ , White – Air). Light is launched into the line-defect waveguide and monitored in the center of the resonator.



**Figure 4.2.** Envelope of the y-component of the electric field in the center of the photonic crystal resonator. Solid red line: Time response of the unmodulated resonator. Blue dashed line: Time response of the modulated resonator. Top: The time dependence of the index of refraction of the background material.

The 2D FDTD simulation is performed by sending a 500-fs gaussian pulse at the resonant wavelength (1525nm) into the line defect waveguide. The wavelength conversion is achieved by reducing the index of the entire background material ( $n=2.75$ ) by  $\Delta n=0.01$  once the field in the resonator has reached its maximum (to enable the maximum amount of light coupled into the resonator to be converted). Here the index is reduced linearly over a 250 fs period starting at  $t=3$ ps and ending at  $t=3.25$ ps. The index is maintained at  $n=2.74$  after the reduction as seen at the top of Figure 4.2. The time response of the field in the resonator with this index modulation is shown as the blue dashed line in Figure 4.2. As seen, it follows the time response of

the unmodulated cavity (red solid line) almost exactly, indicating that no light has been lost as a result of the refractive index tuning. In addition, the light decays from the resonator at the same exact rate, in turn, indicating that the light is still somehow on resonance.



**Figure 4.3.** Spectra of the light in the resonator in the unmodulated (red solid line) and the modulated (blue dashed line) cases. A wavelength shift of  $\Delta\lambda=-5.2$  nm is obtained when the index is reduced by  $\Delta n=-0.01$ .

The reason the light is still on resonance is because the wavelength of the light is being changed in order to stay on resonance with the cavity. This is seen in Figure 4.3 which shows the spectrum of the light in the resonator for the modulated (blue dashed line) and unmodulated (red solid line) cases. Both spectra are obtained by taking the discrete fourier transform (DFT) of the time response shown in Figure 4.2 after the index has been reduced (i.e. after  $t=3.25$  ps). As seen, when the index is reduced by  $\Delta n=-0.01$  the wavelength of the light in the resonator is completely shifted by  $\Delta\lambda=-5.2$  nm and there is no light at the original wavelength (red solid peak).

Therefore, all of the light has been converted to a new wavelength by tuning the photonic crystal resonator. It was also verified that state of the resonator and the new wavelength are the same. In addition, we performed the simulation for many different refractive index changes and found that any wavelength can be generated (i.e.  $\Delta\lambda/\lambda = \Delta n/n$ ). Lastly, we found that this process is independent of the tuning rate, with the simple caveat that the change has to occur while the light is still in the resonator since it is continuously leaking out as seen in Figure 4.2. This fact directly proves that this process is fundamentally different from the spectral distortion effects induced by Kerr non-linearities or high speed modulations. We should note that there is an upper limit on the tuning rate in order to preserve adiabaticity as will be discussed in the next chapter.

In order to understand why this effect is occurring consider the one-dimensional dispersion relation for light:

$$\omega(t) = \frac{c}{n(t,z)} k(z) \quad (4.1)$$

where  $\omega$  is the lights frequency,  $c$  is the speed of light,  $n$  is the refractive index of the medium,  $k$  is the wave number ( $2\pi/\lambda$ ),  $t$  is time and  $z$  is distance. It is clear from this equation that if the refractive index changes only with time then the frequency of the light has no choice but to change because the speed of light is fixed and the spatial wavelength is fixed. Therefore, this simple dispersion relation is the basis for why the frequency of the light changes when the refractive index of the cavity is changed. We see this is the case for all waveforms in the following derivation starting from a one-dimensional wave equation [75]:

$$\frac{\partial^2 E}{\partial x^2} - (\epsilon_o - \epsilon(t))\mu_o \frac{\partial^2 E}{\partial t^2} = 0 \quad (4.2)$$

where  $\varepsilon(t)$  is the time dependent dielectric function. Now consider that we have a wave packet with an electric field described by  $E(t)=f(t)e^{i(k_0x-\omega_0t)}$ , we have:

$$-k_o^2 f - (\varepsilon_o - \varepsilon(t))\mu_o \left( \frac{\partial^2 f}{\partial t^2} - 2i\omega_o \frac{\partial f}{\partial t} - \omega_o^2 f \right) = 0 \quad (4.3)$$

And with the slowly varying amplitude approximation (i.e.  $d^2f/dt^2$  is small):

$$-k_o^2 f - (\varepsilon_o - \varepsilon(t))\mu_o \left( -2i\omega_o \frac{\partial f}{\partial t} - \omega_o^2 f \right) = 0 \quad (4.4)$$

After some simple algebra we have:

$$-i \frac{\partial f}{\partial t} = \frac{\varepsilon(t)\omega_o}{2(\varepsilon(t) + \varepsilon_o)} f \approx \frac{\varepsilon(t)\omega_o}{2(\varepsilon_o)} f \quad (4.5)$$

And this can be solved with the analytical solution:

$$f(t) = f(t_o) e^{i \int_{t_o}^t \frac{\varepsilon(t)\omega_o}{2(\varepsilon_o)} dt} \quad (4.6)$$

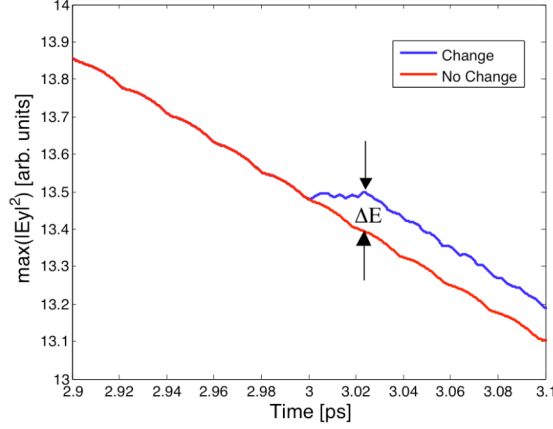
Therefore, the electric field has an instantaneous frequency of:

$$\omega(t) = \omega_o \left( 1 - \frac{\varepsilon(t)}{2\varepsilon_o} \right) \quad (4.7)$$

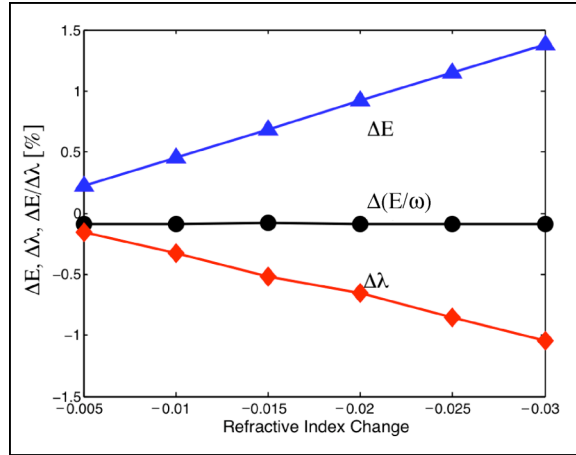
We see from this result that the frequency of the light follows the refractive index change directly, regardless of the speed of the dielectric change. The only requirement for this process is that the light is still in the system during the change and that the index change is transitionally invariant. We note that this process is fundamentally different from traditional frequency generation processes such as sum or different frequency generation. In sum or different frequency generation a field with a frequency of  $\omega_2 - \omega_1$  is needed in order to change the frequency of the light from  $\omega_1$  to  $\omega_2$ . We see from Eq. 4.7 that with this new technique any frequency can be generated with a corresponding refractive index change.

Now we turn to the topic of energy conservation for this wavelength conversion process. Consider Figure 4.4 where we show a zoom in of the envelope of the intensity in the cavity as shown in Figure 4.2. At  $t=3ps$  the refractive index is

changed from 2.75 to 2.74. We see that the energy in the cavity actually steps up when the refractive index is reduced. However, one would have expected the opposite, since the energy of a mode goes as  $E \sim n^2 |E_y|^2$  ( $n$  was reduced so  $E$  should have reduced).



**Figure 4.4.** Zoom in of field shown in Figure 4.2 during the refractive index change at  $t=3\text{ps}$ . It is clear that the energy in the cavity increases during the wavelength conversion process when the refractive index reduces.



**Figure 4.5.** Change in energy in the cavity, change in wavelength and change in  $E/\omega$  for different refractive index reductions. This shows that  $\Delta(E/\omega)$  is an adiabatic invariant.

We can explain this result by investigating Figure 4.5 where we show the change in energy in the cavity and the change in wavelength for different refractive index reductions. From this we see that the energy in the cavity continually increases as the wavelength is changed to shorter and shorter wavelengths. In fact, the energy in the cavity increases by the same amount as the change in wavelength so that the ratio  $E/\omega$  remains exactly the same, as plotted in Figure 4.5. Therefore  $E/\omega$  is a conserved quantity for this wavelength conversion process. This ratio can be understood from classical mechanics by the action integral, which is a measure of the evolution of a system:

$$\begin{aligned}
J &= \oint p \cdot dq \\
H &= \frac{p^2}{2m} + \frac{1}{2} m \omega^2 q^2 \\
J &= \pi \cdot p_{\max} \cdot q_{\max} = \pi \sqrt{2mE} \sqrt{\frac{2E}{m\omega^2}} = 2\pi E/\omega
\end{aligned} \tag{4.8}$$

where  $p$  is the momentum,  $q$  is the spatial coordinate,  $H$  is the Hamiltonian for a harmonic oscillator,  $\omega$  is the oscillator frequency,  $m$  is the mass and  $E$  is the energy. The action integral is calculated over one oscillation and is computed directly as the product of the maximum momentum and maximum displacement. We see that the action integral gives the same result of  $E/\omega$  and is well known in classical mechanics as being an adiabatic invariant for classical oscillators which undergo an adiabatic change [76]. Consequently, the wavelength conversion process presented here is also an adiabatic process. We can understand the significance of  $E/\omega$  by calculating the adiabatic invariant for two different states of the photonic resonator:

$$\frac{E_1}{\omega_1} = \frac{E_2}{\omega_2} \Rightarrow \frac{N\hbar\omega_1}{\omega_1} = \frac{N\hbar\omega_2}{\omega_2} \Rightarrow N = N \tag{4.9}$$

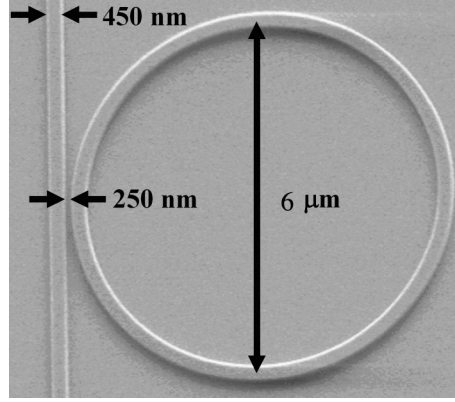


where  $N$  is the number of photons in the mode,  $\omega_{1,2}$  is the frequency of the light, and  $\hbar$  is Planck's constant. Thus, as the photonic crystal is modified from one state to another the number of photons will remain constant. This result ignores any loss of photons as a result of the finite quality factor of the resonator. The implication of the adiabatic invariant is that the adiabatic wavelength conversion process itself is inherently lossless (i.e. all photons are converted to the new state). We should note that this is fundamentally different from sum/difference frequency generation processes where the number of photons must follow  $N_3\hbar\omega_3 = N_1\hbar\omega_1 + N_2\hbar\omega_2$ .

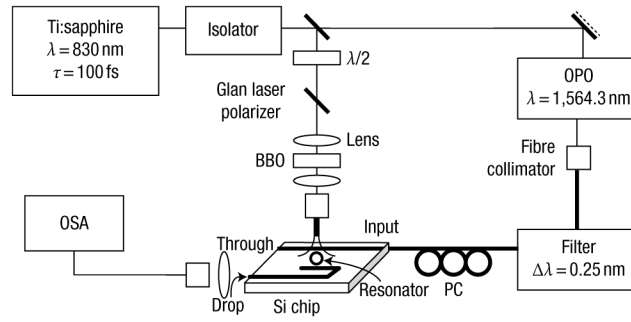
### 4.3 EXPERIMENTAL METHODS

The only requirement for the adiabatic wavelength conversion process is that the resonator is modified in a time scale much shorter than the photon lifetime [75-77]. Until only recently most on-chip resonators had a photon lifetime on the order of a picosecond making it extremely difficult to meet this requirement for the wavelength conversion process. However, we recently demonstrated the ultra-fast tuning of compact silicon ring resonators with photon lifetimes of tens of picoseconds making the work presented here possible [16, 17]. The cavity used here to change the frequency of incoming light is a 6- $\mu\text{m}$ -diameter silicon ring resonator with a waveguide cross-section of 0.45 by 0.25 microns similar to the one seen in Figure 4.6 [17]. Unlike the resonator in Figure 4.6 we use an add/drop configuration here where an additional waveguide is added adjacent to the ring as seen in Figure 4.8e. This additional waveguide is known as the drop port. The ring resonator is measured to have free spectral range (FSR) of  $\text{FSR} = 29.1 \text{ nm}$ , corresponding to a group index of  $n_g=4.45$  [30]. The quality-factor is  $Q \cong \lambda_0/\Delta\lambda_{FWHM} = 18614$ , where  $\lambda_0 = 1,563.3 \text{ nm}$  is the resonance wavelength, and  $\Delta\lambda_{FWHM} = 0.084 \text{ nm}$  is the resonance full-width-at-half-

maximum. This Q-factor corresponds to a photon lifetime of  $\tau_{ph} = \lambda_0^2 / (2\pi c \Delta\lambda_{FWHM}) = 15.5$  ps, where  $c$  is the speed of light in vacuum [17].



**Figure 4.6.** Scanning electron micrograph of a silicon ring resonator side-coupled to a waveguide (adapted from [17]).



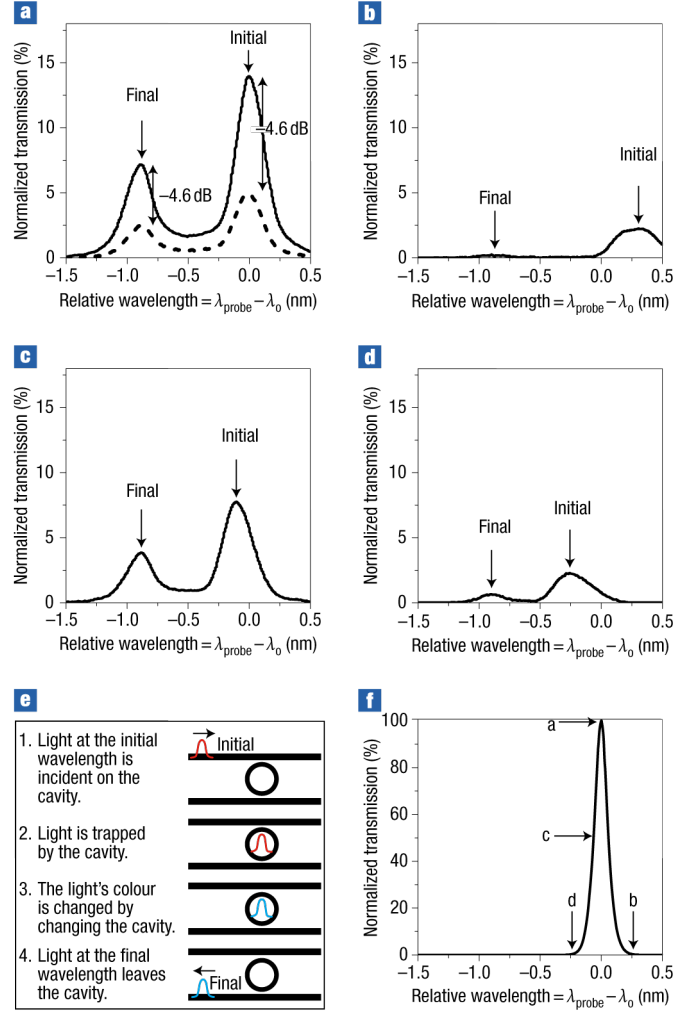
**Figure 4.7.** Experimental set-up used to measure the wavelength-conversion process. OSA, optical spectrum analyser; PC, polarization controller; OPO, optical parametric oscillator; BBO, beta-barium borate crystal. The pump (illuminating the top of the resonator) is used to induce a dynamic change in the cavity, while the probe light (supplied by the OPO) is confined in the ring resonator (from [78]).

In order to induce a fast dynamic change in the resonator, we generate a refractive index change using free-carrier injection. The carrier concentration is induced using short optical pump pulses, however the injection of carriers can also be

achieved electrically [43]. As seen in Figure 4.7, the optical pump is incident on the top of the ring resonator and is linearly absorbed, which generates free-carriers. The free-carriers cause the ring's refractive index to reduce and in turn causes the resonators resonance to blue shift [17, 25]. This resonance shift causes the wavelength of probe light confined in the resonator to also blue-shift by the same amount as depicted in Figure 4.8e.

The experimental setup is seen in Figure 4.7. The pump source is a mode-locked Ti:Sapphire laser that generates 100-fs pulses at 830 nm with 5 nJ of energy at a  $R_{\text{pump}}=76.47$  MHz repetition rate. A beta-barium-borate (BBO) crystal is used to generate second-harmonic pulses centered at  $\lambda_{\text{pump}} = 415$  nm. At this wavelength, the strong linear absorption in silicon causes 90% of the photons transmitted into the 250 nm thick silicon layer to be absorbed [17]. After SHG, the pump pulses are coupled into a short (less than 10 inch) SMF-28 fiber and then exit the output facet, which is placed close to the top surface of the resonator. The energy of the pulse incident on the ring resonator plane is less than 25 pJ. The Ti:Sapphire also pumps an Optical Parametric Oscillator (OPO), which produces the probe pulses. The probe pulses are passed through a  $\Delta\lambda=0.25\text{nm}$  filter (pulse duration measured and theoretically calculated to be approximately  $\tau_{\text{An}}=18$  ps), then polarized and coupled into the silicon waveguide by an external tapered-lensed fiber and an on-chip fiber-to-waveguide nanotaper coupler [17]. The quasi-TE (quasi-TE was chosen over quasi-TM due to its higher Q) light coupled into the ring resonators drop port is then coupled into a fiber by a lens/collimator and then detected by an optical spectrum analyzer (OSA). The pump and probe pulses are aligned in time so that the leading edge of the pumps pulse occurs when probe amplitude in the resonator is at a maximum.

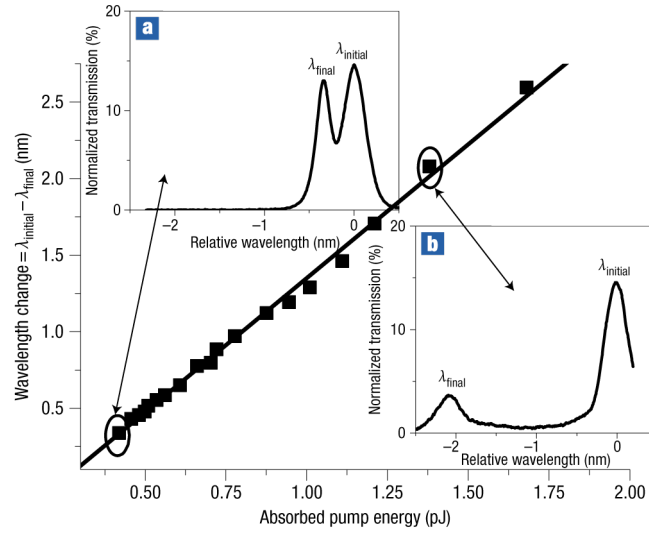
#### 4.4 RESULTS/DISCUSSION



**Figure 4.8.** Wavelength conversion dependence on cavity detuning. **a–d**, Transmission spectra for four different detunings of the incident probe light wavelength relative to the cavity mode. Maximum conversion occurs when the probe is tuned to be on resonance, the dashed line is when the probe input power is reduced by 4.6 dB (**a**). The final wavelength is determined only by the degree of dynamic cavity change. **e**, Illustration of the wavelength-conversion process. **f**, The peak

transmission of the probe when the pump is off. The four initial probe wavelengths (**a-d**) are indicated. (from [78])

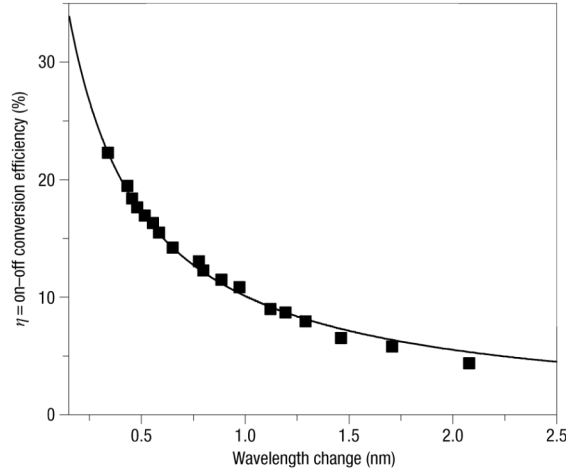
In Figure 4.8a-d we show the normalized probe transmission for four different detunings (indicated as a-d on Figure 4.8f) of the incident probe light wavelength relative to the initial cavity mode,  $\lambda_{\text{probe}} - \lambda_0$ . The probe transmission is normalized to the peak transmission of the probe when the pump is off (shown in Figure 4.8f). The pump energy is fixed in these four figures. When the probe is in resonance or close to resonance with the cavity mode (Fig. Figure 4.8a and Figure 4.8c, respectively), a high degree of light is converted from the initial to the final wavelength. When the initial wavelength of the probe is detuned from the resonance (seen in Figure 4.8b and Figure 4.8d) very little light is converted because very little is initially coupled into the resonator. One can see that the final wavelength is the same in all of these cases and is consequently independent of the initial one. This is because the converted wavelength is determined only by the final state of the resonator, which is fixed in these four examples because the pump energy is fixed. In addition we verified that the final wavelength was in fact the same as the final state of the resonator using a temporally delayed probe pulse. It is also seen in Fig. Figure 4.8a (dashed) that when the probe input power is reduced by 4.6dB the measured transmitted probe signal is also reduced by the same amount and is otherwise unchanged, indicating that the probe itself does not induce any non-linearities.



**Figure 4.9.** Dependence of the measured wavelength change with the absorbed pump energy (square dots – measured, solid line – linear fit). **a-b**, The insets show the transmitted probe power vs. wavelength relative to the initial cavity resonance for absorbed pump energies of 0.419 pJ (upper-left inset,  $\lambda_{\text{initial}} - \lambda_{\text{final}} = 0.339$  nm, Induced Carrier Concentration  $\Delta N = 1.65 \times 10^{17} \text{ cm}^{-3}$ ) and 1.38 pJ (lower-right inset,  $\lambda_{\text{initial}} - \lambda_{\text{final}} = 2.08$  nm, Induced Carrier Concentration  $\Delta N = 1.39 \times 10^{18} \text{ cm}^{-3}$ ), respectively. (from [78])

In contrast to other processes demonstrated to date for wavelength conversion such as Raman-based [72] and four wave mixing [69-71], the change in wavelength is solely determined by the pump intensity and not by the pump or probe wavelengths. This is because the wavelength change is determined solely by the resonance tuning of the ring [76, 77], which is controlled by the injected free carrier concentration. In Figure 4.9 we show the linear dependence of wavelength change with the absorbed pump energy (square dots – measured, solid line – linear fit). The insets show the probe power vs. wavelength relative to the initial cavity resonance for absorbed pump energies of 0.419 pJ (upper-left inset,  $\lambda_{\text{initial}} - \lambda_{\text{final}} = 0.339$  nm) and 1.38 pJ (lower-right

inset,  $\lambda_{\text{initial}} - \lambda_{\text{final}} = 2.08$  nm). Note that the absorbed pump energy is approximately 7% of the incident pump light, due to the small overlap of the pump beam (spot size diameter of approximately 10 microns) and ring area. This is not a fundamental limitation and can be solved using an in-plane pumping scheme used previously by our group [16]. The slope of the fitted line is equal to 1.75 nm/pJ in close agreement with the theoretical value of  $\lambda_0 C_N \lambda_{\text{pump}} / (n_e h c V) = 1.67$  nm/pJ, where  $\lambda_0$  is the resonant wavelength,  $C_N = 3 \cdot 10^{-21} \text{ cm}^3$  is the approximate free-carrier plasma effect coefficient [25],  $\lambda_{\text{pump}}$  is the pump wavelength,  $n_e = 2.4$  is the resonators effective index [26],  $h$  is Planck's constant,  $c$  is the speed of light and  $V$  is the volume of the ring.



**Figure 4.10.** On/off conversion efficiency dependence on wavelength change. The solid line shows our theoretical calculations and the square dots show our experimental conversion efficiency results. The maximum conversion efficiency (34%) was extrapolated from a fit of the experimental data. Free-carrier absorption reduces the conversion efficiency for increasing wavelength changes. (from [78])

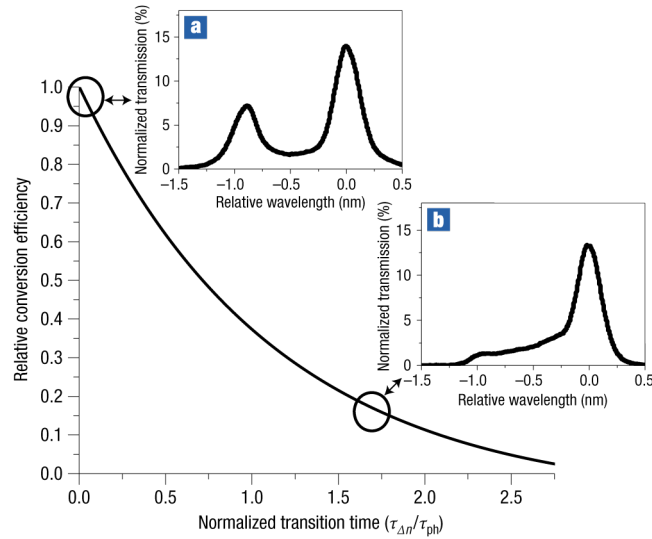
The experimental on/off conversion efficiency is plotted in Figure 4.10 (square dots) as a function of wavelength change. We define the conversion efficiency as

$\eta = 100 \cdot P(\lambda_{\text{final}}) / P_{\text{off}}(\lambda_o) \cdot \Delta\lambda_{\text{final}} / \Delta\lambda_o$  where  $P(\lambda_{\text{final}})$  is the peak probe power at the final wavelength,  $P_{\text{off}}(\lambda_o)$  is the transmitted peak probe power when the pump is off (seen in Figure 4.8f),  $\Delta\lambda_{\text{final}}$  is the FWHM (Full-width Half Maximum) of the probe signal at the final wavelength and  $\Delta\lambda_o$  is the probe FWHM when the pump is off. Note that the FWHM's are included in the efficiency calculation because the bandwidth of the light changes slightly when the pump is on. This is because only a portion of the input probe pulse is converted. Therefore, the light at the initial and final wavelengths has shorter temporal durations than the original input pulse (seen in Figure 4.8f) and consequently larger bandwidths. This will be explained in detail in the next paragraph. In Figure 4.10 it is seen that the conversion efficiency decreases as the wavelength change increases, and correspondingly as the pump power increases (also seen in the insets of Figure 4.9). This is because as more free-carriers are generated more of the light at the final wavelength is absorbed [25]. This is confirmed by calculating the theoretical efficiency (solid line in Figure 4.10) as given by  $\eta = \eta_o \cdot Q_{\text{pump}} / Q_{\text{no-pump}}$ , where  $Q_{\text{pump}} = \pi n_g / \lambda_o \alpha$  is the cavities quality factor in the presence of free-carriers [73],  $Q_{\text{no-pump}} = 18614$  is the quality factor with no pump and  $\eta_o = 34\%$  is a fitting parameter verified using FDTD simulations,  $\alpha$  is the roundtrip loss in the ring resonator and is given by  $\alpha = \alpha_{\text{no-pump}} + \alpha_{\text{pump}}$  where  $\alpha_{\text{no-pump}} = 4.81 \text{ cm}^{-1}$  is the inherent loss of the ring and  $\alpha_{\text{pump}} = 14.5 \cdot 10^{-18} \cdot \Delta N = 14.5 \cdot 10^{-18} \cdot E_{\text{pump}} \cdot \lambda_{\text{pump}} / (hcV) [\text{cm}^{-1}]$  is the loss induced by the free-carriers where  $E_{\text{pump}} = (\lambda_{\text{initial}} - \lambda_{\text{final}}) / 1.75 [\text{pJ}]$  is the absorbed pump energy [25, 26].

The theoretical efficiency of the wavelength conversion process is 100% as was discussed in the previous theory section [76, 77]. However, this is only the efficiency for the light that is in the resonator during the conversion process. In reality not all of the probe pulse can be in the resonator during the conversion process. Here only a maximum of 34% of the pulse was actually in the resonator. Some of the light



at the leading edge of the pulse leaks out of the ring before the conversion process begins, which is clearly seen as the light at the initial wavelength in Figure 4.8a (and in the insets of Figure 4.9). In addition, the light at the trailing edge of the probe pulse which hasn't yet entered the ring resonator when the conversion occurs can't be converted because the ring resonator is now not on resonance with that light. This problem was recently addressed by Gaburro et. al who proposed a solution based on a coupled resonator waveguide in order to ensure a larger portion of the probe pulse is in the system during the conversion [79].



**Figure 4.11.** Relative conversion efficiency as a function of the cavities transition time from its initial to final state. The transition time is normalized to the photon lifetime of the cavity. The solid line is an exponential decay fit to data calculated using two-dimensional finite difference time domain simulations. **a-b**, The insets show the measured probe power with two different pump pulse durations (cavity transition times). (from [78])

As discussed earlier the only requirement for the adiabatic wavelength conversion process is that the light remains in the cavity during the dynamic tuning of the cavities state. Or in other words the tuning time should be much shorter than the photon lifetime of the cavity [77]. This is seen in Figure 4.11 where the relative conversion efficiency as a function of the cavities transition time from its initial to final state (normalized to the lifetime of the cavity) is plotted. The curve was calculated using FDTD simulations. One can see that the  $e^{-1}$  point of the curve is approximately at the point where the index change time is equal to the photon lifetime, as expected. In the inset we show two experimental transmission spectra, one where the pump pulse is sent through a short 10 inch piece of SMF28 fiber and another obtained by sending the pump through 3.5 meters of fiber in order to lengthen the duration of the pump pulse to be on the order of the photon lifetime of the cavity. In the latter case it is seen that there is significantly less light at the final state and it is spread out from the initial to the final state of the resonator. This is because the light is continuously leaking out during the slow conversion process. This fact illustrates that the wavelength of the light confined in the resonator directly follows the state of the resonator. These results point out that in order to get a significant power conversion at the final wavelength in this device the cavity change needs to occur in a time scale less than 10 psec. This requirement can be relaxed using a higher Q cavity [13, 80]. We should note that in this work the Q of the device does decrease slightly due to free-carrier absorption [25, 30, 73]. However, it never reduces enough for the cavity transition used here (100 fs) to not be fast enough.

#### 4.5 SUMMARY

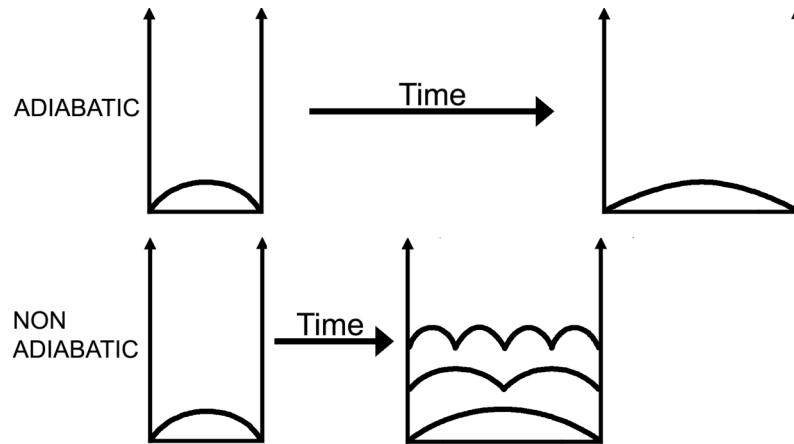
In conclusion we demonstrated a new technique for changing the wavelength of light – adiabatic wavelength conversion where the state of a cavity is dynamically tuned. Here a ring resonator cavity was tuned by injecting free-carrier optically. In the future carriers could be injected or extracted on the required time-scales using recently demonstrated PIN diode electro-optic modulators [26, 27]. This work could open the door to a chip-based wavelength division multiplexing system where a large range of wavelengths could be generated from a single light source at a single wavelength. A wavelength change of up to 2-3 nm was demonstrated but much larger wavelength shifts could be obtained by cascading multiple devices. The ability of dynamically tuning the properties of a resonator could also enable the stopping of light as was pointed out recently by Yanik et al[75, 81]. Note that in this work free-carrier absorption limits the conversion efficiency as the wavelength change increases. In future devices this absorption loss could be counteracted by gain or by extracting the carriers using a reverse-biased diode [26, 42, 70].

## CHAPTER 5

### NON-ADIABATIC WAVELENGTH CONVERSION: PHOTONIC TRANSITIONS

#### 5.1 INTRODUCTION

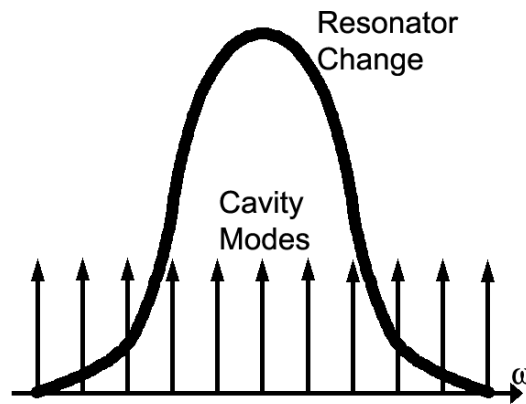
It is well known that light can be generated by direct electronic transitions in an atom, quantum well, quantum dot, or in general between quantized electronic states. The modes of an optical cavity are also quantized, their separation in frequency being inversely proportional to the size of the cavity. However, it is commonly believed that it isn't possible to transition light from one resonant mode to another linearly independent mode. In this chapter we show experimentally that it is indeed possible to induce direct photonic transitions between modes of a cavity, in analogy to electronic transitions in an atom [82] or in a quantum well [83]. This is achieved by using ultra-fast tuning of the refractive index of the cavity over a time interval that is comparable to the inverse of the frequency separation of modes.



**Figure 5.1.** Illustration of the adiabatic and non-adiabatic wavelength conversion process using an infinite potential well analogy.

In the previous chapter we demonstrated adiabatic wavelength conversion where the wavelength of light confined in the resonator was changed by dynamically tuning the resonators state. An illustration of this process, using an infinite potential well as an analogy, is shown at the top of Figure 5.1. We see that as the size of the well is slowly increased the wavelength of the mode simply increases. At the bottom of the same figure we see that when the size of the well is increased much more quickly then many other states are excited. This is the basis for the non-adiabatic wavelength conversion process presented in this chapter.

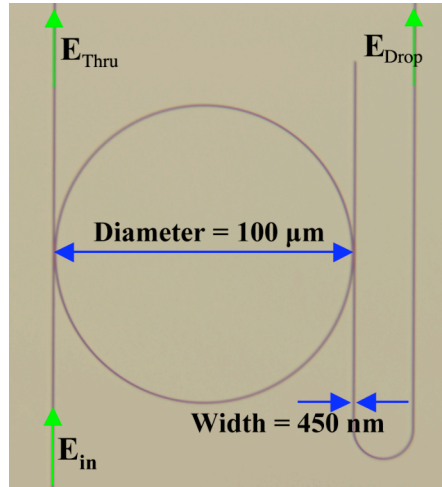
The only requirement for inducing a photonic transition is that the resonator is changed in a time much shorter than the inverse of the frequency separation of the modes. This point is illustrated in Figure 5.2 where we see that the spectral response of the change in the resonator overlaps several of the cavities modes. In this case the necessary fourier components for the transition are large enough in order to transfer substantial amounts of energy from one mode to another. If the resonator change were too slow it would have a much narrower spectral signature which would overlap only a single cavity mode and just result in a small adiabatic change.



**Figure 5.2.** Illustration that the spectral response of the resonators change must overlap many of the cavities modes in order to induce photonic transitions.

We should note that transitions between optical modes were previously observed using a modulator in large optical cavities, for example in frequency comb generators [84] and mode-locked lasers [85]; however, the spacing between the modes is quite small, typically less than 50 GHz, since the cavities are so large. Here in contrast we show the effect for the first time in ultra-compact cavities in which the modes are very far from each other, approximately one order of magnitude farther than in previously demonstrated macroscopic systems.

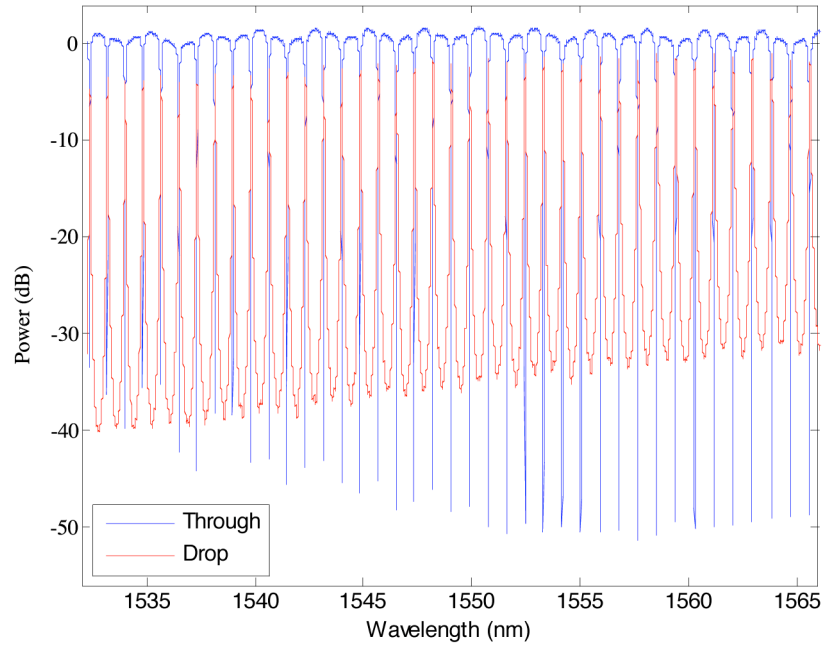
## 5.2 DEVICE



**Figure 5.3.** Microscope image of the large ring resonator with input, thru and drop ports (from [86]).

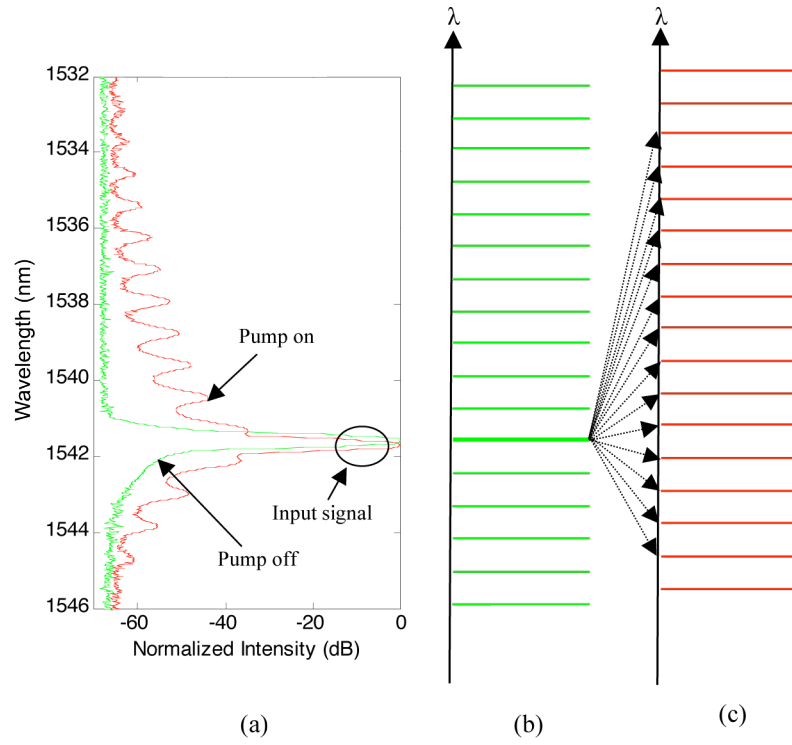
In the previous chapter we demonstrated adiabatic wavelength conversion using a 6  $\mu\text{m}$  ring resonator that had a mode spacing of 29.1nm. However, no photonic transitions were observed because the modes were spaced too far apart. Here we demonstrate photonic transitions using a larger 100  $\mu\text{m}$  ring resonator that has a mode spacing of only 1.9nm (237 GHz). This mode spacing is small enough that transitions

to several modes can be observed. The photonic transitions are induced with the same pump laser used in the previous chapter where 100-fs pump pulses (2 THz) induce a refractive index change in the cavity. The probe signal is supplied by a tunable continuous-wave laser. A microscope image of the ring resonator is shown in Figure 5.3 and the quasi-TM transmission of the through and drop ports of the device are shown in Figure 5.4. The full width at half maximum bandwidth of the resonances is 0.13 nm, which results in a quality factor  $Q=12,000$ . This quality factor corresponds to a photon lifetime of approximately 10 ps.



**Figure 5.4.** Quasi-TM transmission of the through and drop ports of the ring resonator.

### 5.3 RESULTS/DISCUSSION



**Figure 5.5.** Demonstration of photonics transitions (a) Spectrum of the drop port measured for a ring resonator with a radius of 100  $\mu\text{m}$ . A band-pass filter is used to eliminate amplified spontaneous emission noise of the input probe laser. The green line shows the reference spectrum when pump is off, and the probe beam is on one of the rings resonances. The red line shows the spectrum when the pump is on and demonstrates that the input light is transitioned to 15 of the ring resonators adjacent states (c) The diagram of the discrete cavity states of an optical microcavity before (b) and after (c) pump is incident on the sample. The diagram illustrates that light is transition from one state to many other states when the resonator is dynamically tuned. (from [86])



In Figure 5.5a we show the spectra of the transmitted light initially resonant with one of the ring's resonance wavelengths when the pump is off (green line) and when it is on (red line). It is seen that when the pump laser is turned on, 15 new wavelengths are generated, all of which are located at the new resonances of the ring resonator. This uniquely demonstrates that photonic transitions between different cavity modes have been realized in this silicon microcavity. The furthest mode has a wavelength blueshift of more than 8nm from the initial wavelength. A schematic drawing of this process is shown Figure 5.5b and c illustrating that light is transitioned from the initially excited cavity mode to the 15 other modes by the dynamic tuning of the cavity's refractive index.

In order to understand the mechanism of the photonic transitions, one can follow a derivation similar to the time-dependent theory of electronic transitions in quantum mechanics, thanks to the similarity of Maxwell's equations and the Schrödinger equation, to obtain the probability amplitudes for the optical modes [87, 88]:

$$i \frac{d}{dt} a_m(t) = \sum_n V_{mn}(t) a_n(t) \exp[i(\omega_m - \omega_n) \cdot t] \quad (5.1)$$

where  $a_m(t)$  is the amplitude of the  $m$ th-order cavity mode of the resonator associated with an eigenvalue of angular frequency  $\omega_m$ . Furthermore, we assume here that the perturbation of index will not modify the unperturbed cavity modes. This is a valid assumption for the relatively small refractive index changes induced in this experiment. The matrix elements  $V_{mn}(t)$  describe the coupling between different modes when a perturbation is applied on this system. These are given by [87, 88]:

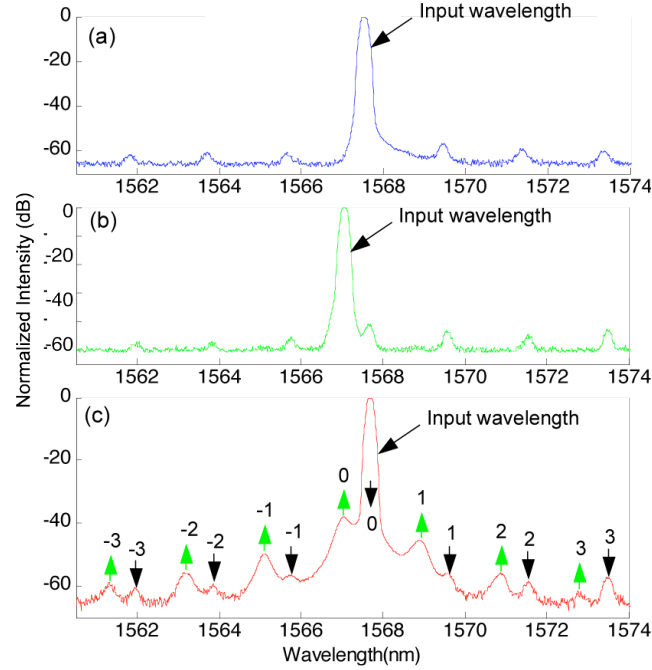
$$V_{mn} = -\frac{\omega_n \mu}{(2\pi)^3} \int d^3 \mathbf{r} \frac{\delta \epsilon(\mathbf{r}, t)}{\epsilon} \mathbf{H}_m^* \cdot \mathbf{H}_n \quad (5.2)$$

Here  $\mathbf{H}_m$  is the magnetic field of the  $m$ th-order cavity mode,  $\mu$  is the permeability constant,  $\epsilon$  is the dielectric function of unperturbed system and  $\delta\epsilon(\mathbf{r},t)$  is the time and spatial dependent perturbation of the dielectric function. We see that in order to induce photonic transitions, the spatial part of  $\delta\epsilon(\mathbf{r},t)$  must produce a non-vanishing integral in Eq. (5.2). Since  $\mathbf{H}_m$  and  $\mathbf{H}_n$  are orthogonal for  $m \neq n$ , this can only be realized by a non-uniform spatial dielectric change. In order to satisfy the condition of non-uniform spatial dielectric change, when the ring is illuminated by the pump care is taken to ensure that the spot size of the pump beam only overlaps a portion of the ring. Additionally, as deduced by Eq. 5.1, the temporal variation of  $\delta\epsilon(\mathbf{r},t)$  must have a non-zero Fourier component near the transition frequency (defined as  $\Delta\omega = \omega_m - \omega_n$ ). To achieve this condition, one can modulate the index at a frequency equal to  $\Delta\omega$  resulting in resonant transitions [87, 88], which is exactly the case of interband transitions in photonic crystals [88]. Alternatively, one could use an ultra-fast index change where the frequency bandwidth of the time-dependent index change overlaps  $\Delta\omega$  as illustrated in Figure 5.2. This condition can be approximated as  $\tau_c \sim 1/\Delta\omega$ , where  $\tau_c$  is the time to complete the index change. In the experiment here we achieve an index change in a time scale of the order of 100 fs, corresponding to the inverse of a frequency of the order of 1THz, spanning a number of cavity modes separated by  $\sim 100$  GHz.

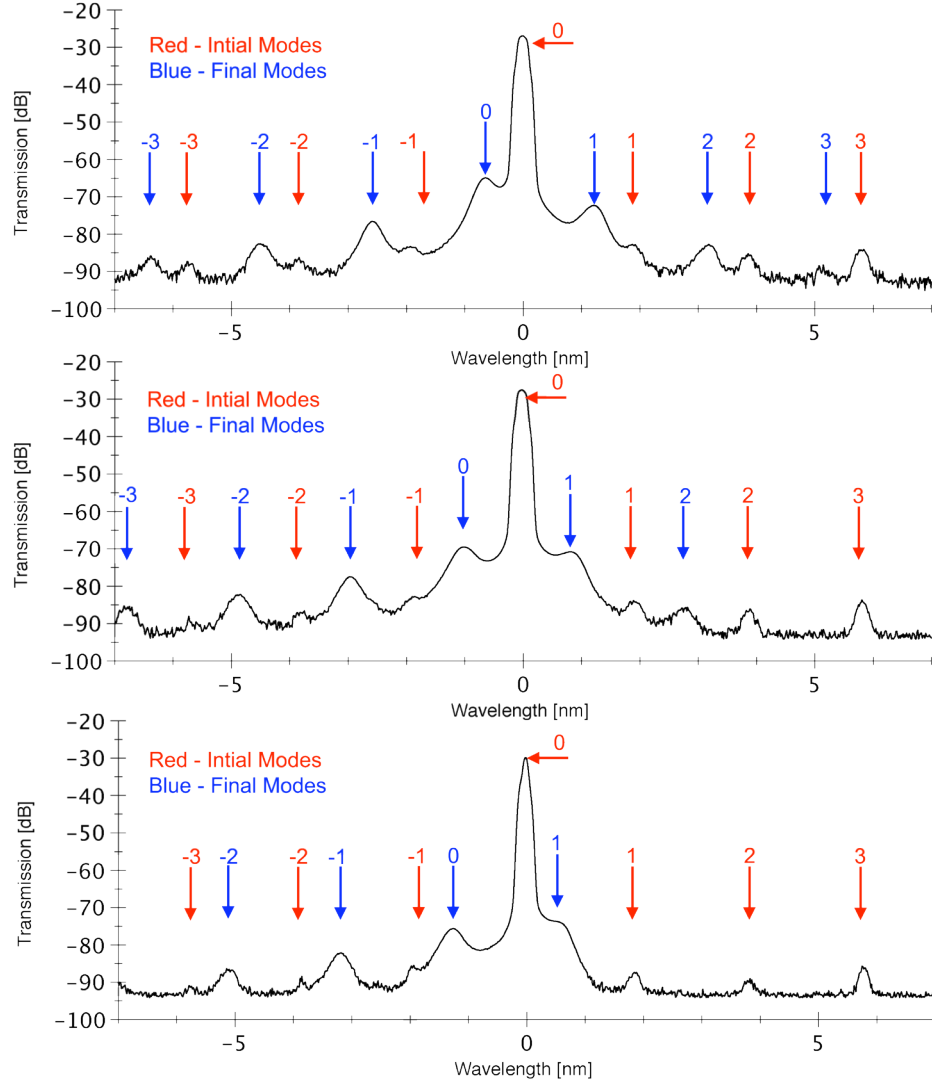
In order to verify the influence of the ring resonator on the measured spectrums here we investigate the results for several different pump/probe configurations. In Figure 5.6a, we show the spectrum of the transmitted light when the pump is off and the probe wavelength is set to be on resonance. The large peak near 1567.5 is the initial mode of the cavity directly excited by the CW laser; the other peaks are a result of the background amplified spontaneous emission (ASE) noise of the CW laser.

These peaks provide a reference for all of the other cavity modes in the spectral range under consideration. In Figure 5.6b the pump is turned on, however the incident probe light is tuned to be off-resonance with the ring resonator. Here we see no sign of conversion to new wavelengths despite the modulation of the cavity's dielectric function by the pump beam. This is due to the fact that since no resonant mode is excited by the input wavelength, there can be no transition to other states (ASE excitation of the resonances is too weak). However, as we tune the input wavelength to be on resonance with the ring, seven new wavelengths appear at the new resonances of the cavity, indicated by green arrows in Figure 5.6c. This uniquely demonstrates that all of the new wavelengths are generated by conversion of the initial probe state to the new photonic states. Note in Figure 5.6c that the new wavelengths appear at the resonances of the perturbed ring which are slightly blue shifted from the initial states by the induced refractive index change. Since the photon lifetime (10 ps) is much smaller than the carrier recombination lifetime (450 ps) the converted photons leak out from the resonator (and are measured) before the ring returns to its unperturbed state. The 0<sup>th</sup> order conversion comes from the adiabatic transition of initial mode to the perturbed mode of the same order. This adiabatic frequency conversion was investigated in the previous chapter, however, its frequency shift is limited by the index change. In contrast, here the transitions between the modes of different orders do not suffer from this limitation. From Figure 5.6c, the maximum wavelength shift is -6.7 nm, and the absolute conversion efficiencies for the 0th order and -1st order are 0.03% and  $7 \times 10^{-4}\%$  respectively. These conversion efficiencies seem low because the CW probe light is only converted whenever a pump pulse occurs (every 13 ns). Taking this into account and the photon lifetime of the cavity we determine the conversion

efficiency per pump pulse to be approximately 38% for the 0th order mode and 1% for the -1st order.

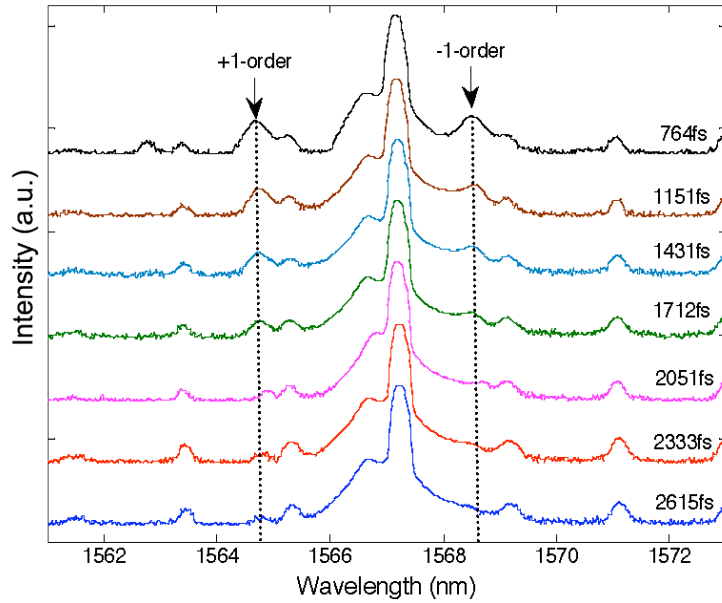


**Figure 5.6.** Cavities influence on photonic transitions a) Spectrum measured at the drop port of the ring resonator when the pump is off. The input wavelength of the CW laser is in resonance with the ring cavity (large peak). The smaller peaks are the other resonances of the ring resonator which are excited by the amplified spontaneous emission noise of the probe laser. b) Spectrum when the pump is turned on. However, the input probe wavelength is detuned from the rings resonance therefore no photonic transitions are evident. c) Same as in (b) but now the input wavelength is in resonance with the ring cavity. Seven new wavelengths appear in the spectrum. The black arrows indicate the original modes and the green arrows indicate the wavelengths generated by the photonic transitions. (from [86])



**Figure 5.7.** Changing the transition probabilities by increasing the cavity tuning. The spectrums for three different cavity tunings (increasing from top to bottom) are shown. It is seen that the amount of light in each of the final modes depends on the degree of cavity tuning (The amount of cavity tuning increases linearly with pump energy). The spectrums are as follows: **(top)** Tuning: 0.66 nm, 0-order efficiency: 19%, 1<sup>st</sup>-order efficiency: 3.6% **(middle)** Tuning: 0.96 nm, 0-order efficiency: 7.5%, 1<sup>st</sup>-order efficiency: 3.7% **(bottom)** Tuning: 1.25 nm, 0-order efficiency: 3.3% 1<sup>st</sup>-order efficiency: 5%.

The amount of light that transitions to a particular mode depends on how far away it is from the initially excited mode as is clearly seen in Figure 5.6. The amount of light in each mode also depends on the degree of cavity tuning as seen in Figure 5.7. As one would expect as cavity modes move closer/further away to the initial mode the transition probability increases/decreases. This is seen in Figure 5.7 where the amount of light in the final 0-order mode decreases and amount of light in the 1<sup>st</sup>-order mode increases as the cavity tuning is increased. We should note that the amount of light in the modes to the left of the initially excited mode is considerably greater than those on the right. This is because the modes are blue-shifted (shifted to the left) by the induced refractive index change and this inherently gives a bias for the transitions to the left.



**Figure 5.8.** Spectra for different pump pulse durations. It is evident that the probability of nonadiabatic transitions increase as the pulse duration becomes shorter. (from [86])

In order to verify that the cavities refractive index has to be changed much faster than the inverse of the frequency spacing of the modes here we measure the transmitted spectrum with several different pump pulse durations. The pump pulse duration is varied by using a two-grating system, in which grating dispersion is introduced to temporally expand the pulse [89, 90]. We see in Figure 5.8, where the spectra for different pulse durations is shown, that the transition probabilities for -1-order and 1-order transitions decrease as the pulse duration increases. This is the case because as the pulse duration increases the frequency bandwidth of the dynamic index change decreases, decreasing the transition probabilities to modes of different orders according to equation 1 and seen in Figure 5.2. We have also demonstrated from this result that as the cavity tuning is slowed it is possible to achieve adiabatic wavelength conversion as demonstrated in the previous chapter.

#### 5.4 SUMMARY

In conclusion, we experimentally demonstrate generation of new frequencies by inducing photonic transitions between discrete modes of a silicon optical microcavity, in analogy to electronic transitions. This effect allows the generation of new wavelengths of light in materials such as silicon which are generally not optically active [42, 70]. Additionally, this work could enable on-chip generation of multi-wavelength comb sources that could find numerous applications in sensing, metrology, and optical communications. Amplifiers can be used to boost and equalize the power at the newly generated wavelengths enabling a practical comb source on a chip. By varying the magnitude of the index change and the probe input wavelength the converted wavelengths can be tuned over the entire operational range of the ring resonator which is more than 100nm. In this work, the quality factor of the micro-ring

resonators used is moderate, compared with those photonic crystal microcavities and suspended micro disks or toroids [13, 74]. A larger quality-factor may benefit the conversion efficiency as the trapped light can stay longer in the cavity.



## REFERENCES

1. W. A. Gambling, "The rise and rise of optical fibers," *IEEE Journal of Selected Topics in Quantum Electronics* **6**, 1084-1093 (2000).
2. D. B. Keck, "Method of forming optical waveguide fibers," (Google Patents).
3. M. Taubenblatt, "Opportunities and Challenges for Optics in the Information Processing Industry," in *IBM Executive Symposium on Photonics Commercialization* (IBM T.J. Watson Research Center, 2006).
4. L. C. Kimerling, "Photonics to the rescue microelectronics becomes microphotonics," *Electrochemical Society Interface* **9**, 28-31 (2000).
5. D. A. B. Miller, "Optical interconnects to silicon," *IEEE Journal of Selected Topics in Quantum Electronics* **6**, 1312-1317 (2000).
6. C. Gunn, "CMOS Based Photonic Integration for Optical Interconnects," in *Optical Fiber Conference*(Anaheim, CA, 2007), p. OTuD1.
7. P. Pepeljugoski, F. Doany, D. Kuchta, L. Schares, C. Schow, M. Ritter, and J. Kash, "Data Center and High Performance Computing Intreconnects for 100 Gb/s and Beyond," in *Optical Fibers Conference*(Anaheim, CA, 2007), p. OMR4.
8. C. Schow, F. Doany, O. Liboiron-Ladouceur, C. Baks, D. Kuchta, L. Schares, R. John, and J. Kash, "160-Gb/s, 16-Channel Full-Duplex, Single-Chip CMOS

Optical Transceiver," in *Optical Fiber Conference* (Anaheim, CA, 2007), p. OThG4.

9. ITRS, "International Technology Roadmap for Semiconductors," (2003).
10. V. R. Almeida, R. R. Panepucci, and M. Lipson, "Nanotaper for compact mode conversion," *Optics Letters* **28**, 1302-1304 (2003).
11. M. Lipson, "Overcoming the limitations of microelectronics using Si nanophotonics: solving the coupling, modulation and switching challenges," *Nanotechnology* **15**, S622 (2004).
12. S. Fan, S. G. Johnson, J. D. Joannopoulos, C. Manolatou, and H. A. Haus, "Waveguide branches in photonic crystals," *J. Opt. Soc. Am. B* **18**, 162–165 (2001).
13. B.-S. Song, S. Noda, T. Asano, and Y. Akahane, "Ultra-high-Q photonic double-heterostructure nanocavity," *Nature Materials* **4**, 207-210 (2005).
14. T. Tanabe, M. Notomi, E. Kuramochi, A. Shinya, and H. Taniyama, "Trapping and delaying photons for one nanosecond in an ultrasmall high-Q photonic-crystal nanocavity," *Nature Photonics* **1**, 49-52 (2007).
15. B. E. Little, J. S. Foresi, G. Steinmeyer, E. R. Thoen, S. T. Chu, H. A. Haus, E. P. Ippen, L. C. Kimerling, and W. Greene, "Ultra-compact Si-SiO<sub>2</sub> microring resonator optical channel dropping filters," *Photonics Technology Letters, IEEE* **10**, 549-551 (1998).

16. V. R. Almeida, C. A. Barrios, R. R. Panepucci, and M. Lipson, "All-optical control of light on a silicon chip," *Nature* **431**, 1081-1084 (2004).
17. V. R. Almeida, C. A. Barrios, R. R. Panepucci, M. Lipson, M. A. Foster, D. G. Ouzounov, and A. L. Gaeta, "All-optical switching on a silicon chip," *Optics Letters* **29**, 2867-2869 (2004).
18. F. Xia, L. Sekaric, and Y. Vlasov, "Ultracompact optical buffers on a silicon chip," *Nature Photonics* **1**, 67-71 (2007).
19. M. Borselli, T. Johnson, and O. Painter, "Beyond the Rayleigh scattering limit in high-Q silicon microdisks: theory and experiment," *Optics Express* **13**, 1515-1530 (2005).
20. V. R. Almeida, and M. Lipson, "Optical bistability on a silicon chip," *Optics Letters* **29**, 2387-2389 (2004).
21. G. Cocorullo, and I. Rendina, "Thermo-optical modulation at 1.5  $\mu\text{m}$  in silicon etalon," *Electronics Letters* **28**, 83-85 (1992).
22. G. Cocorullo, M. Iodice, I. Rendina, and P. M. Sarro, "Silicon thermo-optical micromodulator with 700-kHz-3-dB bandwidth," *Photonics Technology Letters, IEEE* **7**, 363-365 (1995).
23. R. Soref, and B. Bennett, "Electro-optical effects in silicon," *Quantum Electronics, IEEE Journal of* **23**, 123-129 (1987).
24. M. Dinu, F. Quochi, and H. Garcia, "Third-order nonlinearities in silicon at telecom wavelengths," *Applied Physics Letters* **82**, 2954-2956 (2003).

25. R. A. Soref, and B. R. Bennett, "Kramers-Kronig analysis of electro-optical switching in silicon," SPIE Integrated Opt. Circuit Eng. **704**, 32-37 (1987).
26. S. F. Preble, Q. Xu, B. S. Schmidt, and M. Lipson, "Ultrafast all-optical modulation on a silicon chip," Optics Letters **30**, 2891-2893 (2005).
27. Q. Xu, S. Manipatruni, B. Schmidt, J. Shakya, and M. Lipson, "12.5 Gbit/s carrier-injection-based silicon micro-ring silicon modulators," Optics Express **15**, 430-436 (2007).
28. D. K. Armani, T. J. Kippenberg, S. M. Spillane, and K. J. Vahala, "Ultra-high-Q toroid microcavity on a chip," Nature **421**, 925-928 (2003).
29. C. Manolatou, M. J. Khan, S. Fan, P. R. Villeneuve, H. A. Haus, and J. D. Joannopoulos, "Coupling of modes analysis of resonant channel add-drop filters," Quantum Electronics, IEEE Journal of **35**, 1322-1331 (1999).
30. A. Yariv, "Universal relations for coupling of optical power between microresonators and dielectric waveguides," Electronics Letters **36**, 321-322 (2000).
31. P. Rabiei, W. H. Steier, C. Zhang, and L. R. Dalton, "Polymer Micro-Ring Filters and Modulators," JOURNAL OF LIGHTWAVE TECHNOLOGY **20** (2002).
32. M. Harjanne, M. Kapulainen, T. Aalto, and P. Heimala, "Sub- $\mu$ s switching time in silicon-on-insulator Mach-Zehnder thermo-optic switch," IEEE Photonics Technology Letters **16**, 2039-2041 (2004).

33. H. W. Tan, H. M. van Driel, S. L. Schweizer, R. B. Wehrspohn, and U. Gösele, "Nonlinear optical tuning of a two-dimensional silicon photonic crystal," *Physical Review B* **70**, 205110 (2004).
34. C. A. Barrios, V. R. de Almeida, and M. Lipson, "Low-power-consumption short-length and high-modulation-depth silicon electrooptic modulator," *Journal of Lightwave Technology* **21**, 1089-1098 (2003).
35. J. T. Robinson, C. Manolatou, L. Chen, and M. Lipson, "Ultrasmall Mode Volumes in Dielectric Optical Microcavities," *Physical Review Letters* **95**, 143901-143904 (2005).
36. J. S. Foresi, P. R. Villeneuve, J. Ferrera, E. R. Thoen, G. Steinmeyer, S. Fan, J. D. Joannopoulos, L. C. Kimerling, H. I. Smith, and E. P. Ippen, "Photonic-bandgap microcavities in optical waveguides," *Nature* **390**, 143-145 (1997).
37. V. R. Almeida, X. Qianfan, C. A. Barrios, and M. Lipson, "Guiding and confining light in void nanostructure," *Optics Letters* **29**, 1209-1211 (2004).
38. S. F. Preble, V. R. Almeida, and M. Lipson, "Optically controlled photonic crystal nanocavity in silicon," (International Society for Optical Engineering, Bellingham, WA 98227-0010, United States, Denver, CO, United States, 2004), pp. 10-17.
39. J. R. Meyer, F. J. Bartoli, and M. R. Kruer, "Optical heating in semiconductors," *Physical Review B (Condensed Matter)* **21**, 1559-1568 (1980).

40. D. B. Laks, G. F. Neumark, A. Hangleiter, and S. T. Pantelides, "Theory of interband Auger recombination in  $n$ -type silicon," *Physical Review Letters* **61**, 1229-1232 (1988).
41. S. F. Preble, V. R. Almeida, and M. Lipson, "All-optical control of light using silicon nanophotonic devices," (Optical Society of America, Washington, DC 20036-1023, United States, Baltimore, MD, United States, 2005), pp. 122-124.
42. H. Rong, R. Jones, A. Liu, O. Cohen, D. Hak, A. Fang, and M. Paniccia, "A continuous-wave Raman silicon laser," *Nature* **433**, 725-728 (2005).
43. Q. Xu, B. Schmidt, S. Pradhan, and M. Lipson, "Micrometre-scale silicon electro-optic modulator," *Nature* **435**, 325-327 (2005).
44. E. Conforti, A. C. Bordonalli, S. Ho, and S.-M. Kang, "Optical 2R remodulator using feedforward control of semiconductor optical amplifier gain," *Microwave and Optical Technology Letters* **21**, 39-42 (1999).
45. J. H. Holland, *Adaptation in Natural and Artificial Systems* (University of Michigan, Ann Arbor, 1975).
46. J. R. Koza, M. A. Keane, M. J. Streeter, W. Mydlowec, J. Yu, and G. Lanza, *Genetic Programming IV. Routine Human-Competitive Machine Intelligence* (Kluwer, Boston, MA, 2003).
47. M. Mitchell, *An introduction to genetic algorithms* (MIT Press, 1996).
48. H. Lipson, and J. B. Pollack, "Automatic design and manufacture of robotic lifeforms," *Nature* **406**, 974-978 (2000).

49. L. Sanchis, A. Hakansson, D. Lopez-Zanon, J. Bravo-Abad, and J. Sanchez-Dehesa, "Integrated optical devices design by genetic algorithm," *Applied Physics Letters* **84**, 4460-4462 (2004).
50. M. M. Spuhler, B. J. Offrein, G. L. Bona, R. Germann, I. Massarek, and D. Erni, "Very short planar silica spot-size converter using a nonperiodic segmented waveguide," *Journal of Lightwave Technology* **16**, 1680-1685 (1998).
51. L. Poladian, S. Manos, and B. Ashton, "Multi-objective and constrained design of gratings using genetic algorithms," (Institute of Electrical and Electronics Engineers Inc., Piscataway, NJ 08855-1331, United States, Tokyo, Japan, 2005), pp. 950-952.
52. S. Kim, G. P. Nordin, J. Jiang, and J. Cai, "Microgenetic algorithm design of hybrid conventional waveguide and photonic crystal structures," *Optical Engineering* **43**, 2143-2149 (2004).
53. S. Linfang, Y. Zhuo, and H. Sailing, "Design of two-dimensional photonic crystals with large absolute band gaps using a genetic algorithm," *Physical Review B (Condensed Matter and Materials Physics)* **68**, 35109-35101 (2003).
54. S. Preble, M. Lipson, and H. Lipson, "Two-dimensional photonic crystals designed by evolutionary algorithms," *Applied Physics Letters* **86**, 061111 (2005).
55. A. Gondarenko, S. Preble, J. Robinson, L. Chen, H. Lipson, and M. Lipson, "Spontaneous emergence of periodic patterns in a biologically inspired simulation of photonic structures," *Physical Review Letters* **96**, 143904 (2006).

56. J. T. Robinson, M. Lipson, and H. Lipson, "Strong light confinement in novel compact pseudo-random structures designed via Evolutionary Algorithms," (Optical Society of America, Washington, DC 20036-1023, United States, Baltimore, MD, United States, 2005), pp. 966-968.
57. E. Yablonovitch, "Inhibited spontaneous emission in solid-state physics and electronics," *Physical Review Letters* **58**, 2059-2062 (1987).
58. S. G. Johnson, and J. D. Joannopoulos, *Photonic Crystals: The Road from Theory to Practice* (Kluwer, Boston, MA, 2002).
59. J. D. Joannopoulos, R. D. Mead, and J. N. Winn, *Photonic Crystals* (Princeton University Press, Princeton, NJ, 1995).
60. L. P. Biro, Z. Balint, K. Kertesz, Z. Vertesy, G. I. Mark, Z. E. Horvath, J. Balazs, D. Mehn, I. Kiricsi, V. Lousse, and J. P. Vigneron, "Role of photonic-crystal-type structures in the thermal regulation of a Lycaenid butterfly sister species pair," *Physical Review E* **67**, 21907-21901 (2003).
61. R. A. Potyrailo, H. Ghiradella, A. Vertiatchikh, K. Dovidenko, J. R. Cournoyer, and E. Olson, "Morpho butterfly wing scales demonstrate highly selective vapour response," *Nat Photon* **1**, 123-128 (2007).
62. R. C. McPhedran, N. A. Nicorovici, D. R. McKenzie, L. C. Botten, A. R. Parker, and G. W. Rouse, "The sea mouse and the photonic crystal," *Australian Journal of Chemistry* **54**, 241-244 (2001).



63. E. Yablonovitch, "Photonic band-gap structures," *Journal of the Optical Society of America B: Optical Physics* **10**, 283-295 (1993).
64. N. Susa, "Large absolute and polarization-independent photonic band gaps for various lattice structures and rod shapes," *Journal of Applied Physics* **91**, 3501 (2002).
65. S. G. Johnson, and J. D. Joannopoulos, "Block-iterative frequency-domain methods for Maxwell's equations in a planewave basis," *Optics Express* **8** (2001).
66. S. W. Mahfoud, "Niching methods for Genetic Algorithms," (University of Illinois, Urbana Champaign, IL, 1995).
67. C. M. Anderson, and K. P. Giapis, "Larger two-dimensional photonic band gaps," *Physical Review Letters* **77**, 2949-2952 (1996).
68. M. Qiu, and S. He, "Large complete band gap in two-dimensional photonic crystals with elliptic air holes," *Physical Review B* **60**, 10610 (1999).
69. R. L. Espinola, J. I. Dadap, R. M. Osgood, Jr., S. J. McNab, and Y. A. Vlasov, "C-band wavelength conversion in silicon photonic wire waveguides," *Optics Express* **13** (2005).
70. M. A. Foster, A. C. Turner, J. E. Sharping, B. S. Schmidt, M. L. Lipson, and A. L. Gaeta, "Broad-band optical parametric gain on a silicon photonic chip," *Nature* **441**, 960-963 (2006).

71. H. Fukuda, K. Yamada, T. Shoji, M. Takahashi, T. Tsuchizawa, T. Watanabe, J. Takahashi, and S. Itabashi, "Four-wave mixing in silicon wire waveguides," *Optics Express* **13** (2005).
72. B. Jalali, V. Raghunathan, D. Dimitropoulos, and O. Boyraz, "Raman-based silicon photonics," *IEEE Journal of Selected Topics in Quantum Electronics* **12**, 412-421 (2006).
73. Q. Xu, V. R. Almeida, and M. Lipson, "Micrometer-scale all-optical wavelength converter on silicon," *Optics Letters* **30**, 2733-2735 (2005).
74. K. J. Vahala, "Optical microcavities," *Nature* **424**, 839-846 (2003).
75. M. F. Yanik, and S. Fan, "Dynamic Photonic Structures: Stopping, Storage, and Time Reversal of Light," *Studies in Applied Mathematics* **115**, 233-253 (2005).
76. M. Notomi, and S. Mitsugi, "Wavelength conversion via dynamic refractive index tuning of a cavity," *Physical Review A (Atomic, Molecular, and Optical Physics)* **73**, 51803-51801 (2006).
77. S. F. Preble, and M. Lipson, "Conversion of a signal wavelength in a dynamically tuned resonator," *Integrated Photonics Research and Applications Topical Meeting, IMC5* (2006).
78. S. F. Preble, Q. Xu, and M. Lipson, "Changing the colour of light in a silicon resonator," *Nat Photon* **1**, 293-296 (2007).
79. Z. Gaburro, M. Ghulinyan, F. Riboli, L. Pavesi, A. Recati, and I. Carusotto, "Photon energy lifter," *Optics Express* **14**, 7270-7278 (2006).

80. M. Loncar, M. Hochberg, A. Scherer, and Q. Yueming, "High quality factors and room-temperature lasing in a modified single-defect photonic crystal cavity," *Optics Letters* **29**, 721-723 (2004).
81. Q. Xu, P. Dong, and M. Lipson, "Breaking the delay-bandwidth limit in a photonic structure," *Nature Phys.*, advanced online publication (2007).
82. M. O. Scully, and M. S. Zubairy, *Quantum Optics* (Cambridge University Press, Cambridge, 1997).
83. P. Harrison, *Quantum wells, wires and dots: theoretical and computational physics* (Wiley, 2000).
84. T. Kobayashi, T. Sueta, Y. Cho, and Y. Matsuo, "High-repetition-rate optical pulse generator using a Fabry-Perot electro-optic modulator," *Applied Physics Letters* **21**, 341-343 (1972).
85. A. Yariv, *Optical Electronics in Modern Communications* (Oxford University Press, 1997).
86. P. Dong, S. F. Preble, J. T. Robinson, S. Manipatrani, and M. Lipson, "Inducing Photonic Transitions between Discrete Modes in a Silicon Optical Microcavity: an Analogue to Electronic Transitions in Atoms," *Nature Photonics* (in review-2007).
87. N. Malkova, S. Kim, and V. Gopalan, "Jahn-Teller effect in two-dimensional photonic crystals," *Physical Review B* **68**, 045105 (2003).

88. J. N. Winn, S. Fan, J. D. Joannopoulos, and E. P. Ippen, "Interband transitions in photonic crystals," *Physical Review B* **59**, 1551 (1999).
89. J.-C. Diels, and W. Rudolph, *Ultrashort Laser Pulse Phenomena* (Academic Press Inc., U.S., 2006).
90. E. B. Treacy, "Optical pulse compression with diffraction gratings," *IEEE J. Quan. Elect.* **QE-5**, 454-458 (1969).